J Neurophysiol 113: 23–43, 2015.
First published September 17, 2014; doi:10.1152/jn.00601.2013.

High-conductance states and A-type K^+ channels are potential regulators of the conductance-current balance triggered by HCN channels

Poonam Mishra and Rishikesh Narayanan
Cellular Neurophysiology Laboratory, Molecular Biophysics Unit, Indian Institute of Science, Bangalore, India

Submitted 23 August 2013; accepted in final form 12 September 2014

Mishra P, Narayanan R. High-conductance states and A-type K^+ channels are potential regulators of the conductance-current balance triggered by HCN channels. *J Neurophysiol* 113: 23–43, 2015. First published September 17, 2014; doi:10.1152/jn.00601.2013.—An increase in the hyperpolarization-activated cyclic nucleotide-gated (HCN) channel conductance reduces input resistance, whereas the consequent increase in the inward *h* current depolarizes the membrane. This results in a delicate and unique conductance-current balance triggered by the expression of HCN channels. In this study, we employ experimentally constrained, morphologically realistic, conductance-based models of hippocampal neurons to explore certain aspects of this conductance-current balance. First, we found that the inclusion of an experimentally determined gradient in A-type K^+ conductance, but not in M-type K^+ conductance, tilts the HCN conductance-current balance heavily in favor of conductance, thereby exerting an overall restorative influence on neural excitability. Next, motivated by the well-established modulation of neuronal excitability by synaptically driven high-conductance states observed under in vivo conditions, we inserted thousands of excitatory and inhibitory synapses with different somatodendritic distributions. We measured the efficacy of HCN channels, independently and in conjunction with other channels, in altering resting membrane potential (RMP) and input resistance (R_{in}) when the neuron received randomized or rhythmic synaptic bombardments through variable numbers of synaptic inputs. We found that the impact of HCN channels on average RMP, R_{in}, firing frequency, and peak-to-peak voltage response was severely weakened under high-conductance states, with the impinging synaptic drive playing a dominant role in regulating these measurements. Our results suggest that the debate on the role of HCN channels in altering excitability should encompass physiological and pathophysiological neuronal states under in vivo conditions and the spatiotemporal interactions of HCN channels with other channels.

computational model; conductance-current balance; HCN channel; high-conductance state; hippocampal pyramidal neuron; transient potassium channel

THE HYPERPOLARIZATION-ACTIVATED cyclic nucleotide-gated (HCN) channels are critical regulators of neuronal physiology. These nonspecific cationic channels mediate the *h* current that, under physiological conditions, stays inward across the entire activation range of the channels. Therefore, activation of these channels results in membrane potential depolarization, taking the neuron closer to action potential threshold. However, unlike most channels that mediate inward currents, HCN channels are activated by hyperpolarization. As a direct consequence of this, activation of these channels would resist changes in membrane potential, thereby reducing the input resistance of the neuron through an overall increase in the membrane conductance (Dyhrfjeld-Johnsen et al. 2009; Gasparini and DiFrancesco 1997; He et al. 2014; Hutcheon and Yarom 2000; Magee 1998; Migliore and Migliore 2012; Narayanan and Johnston 2008; Pape 1996; Robinson and Siegelbaum 2003; Santoro and Baram 2003; Shah 2014). Together, the expression of HCN channels acts to increase neuronal excitability by depolarizing the membrane and taking the neuron closer to firing, and simultaneously acts to reduce neuronal gain through the consequent increase in membrane conductance. Such dichotomous impact of HCN channels on neuronal excitability and the underlying balance between the HCN conductance and the *h* current have been at the center of a wide-ranging debate on the regenerative vs. restorative roles of these channels in regulating neuronal physiology (Breton and Stuart 2009; Chen et al. 2001; Dyhrfjeld-Johnsen et al. 2009; Fan et al. 2005; George et al. 2009; Kim et al. 2012; Lippert and Booth 2009; Magee 1998; Migliore and Migliore 2012; Narayanan and Johnston 2007; Noam et al. 2011; Pavlov et al. 2011; Rosenkranz and Johnston 2006; Santoro and Baram 2003). The analysis of whether HCN channel expression leads to restorative or regenerative effects is central to ascribing homeostatic vs. excitotoxic roles for changes in these channels under several physiological and pathophysiological conditions (Brager et al. 2012; Brager and Johnston 2007; Dyhrfjeld-Johnsen et al. 2009; Fan et al. 2005; Jung et al. 2007; Kole et al. 2007; Lerche et al. 2013; Narayanan et al. 2010; Narayanan and Johnston 2007; Santoro and Baram 2003; Shah 2014; Shah et al. 2004; van Welie et al. 2004). Furthermore, a tilt in the balance between the restorative HCN conductance and the regenerative *h* current as a consequence of coexpressing ion channels, or through any other physiological parameter, will profoundly alter the overall impact of these channels on neuronal excitability and therefore is critical in the design of drugs with HCN channels as potential targets (Brager et al. 2012; Chen et al. 2001; Lerche et al. 2013; Noam et al. 2011; Poolos et al. 2002; Santoro and Baram 2003; Shah 2014, 2012; Shah et al. 2013). Despite such critical importance of the analysis and despite the predominant expression of HCN channels in neuronal dendrites (Kole et al. 2006; Lorincz et al. 2002; Magee 1998; Williams and Stuart 2000), most analyses on the HCN conductance-current balance are driven from a somatic standpoint and are confined to in vitro physiology where afferent activity to a neuron is sparse.

In this study, we asked if interactions with the A-type K^+ (KA) channels altered the conductance-current balance that is consequent to the presence of HCN channels. The rationale behind the choice of KA channels was the large subthreshold window component of the current through these channels, their dendritic localization, and their critical role in the regulation of

Address for reprint requests and other correspondence: R. Narayanan, Molecular Biophysics Unit, Indian Institute of Science, Bangalore 560 012, India (e-mail: rishi@mbu.iisc.ernet.in).

neuronal excitability (Chen et al. 2006; Hoffman et al. 1997; Kim et al. 2005; Migliore et al. 1999), apart from their well-established interactions with the HCN channels across systems (MacLean et al. 2003; Rathour and Narayanan 2014, 2012a; Santoro and Baram 2003). Next, we noted that under in vivo conditions, a neuron receives inputs through several thousands of synapses, leading to what have been referred to as high-conductance states in neurons, which exert profound control on the average resting potential and the gain of the neuron (Chance et al. 2002; Destexhe et al. 2003). Against this, we asked if conclusions on the dichotomous impact of HCN conductance and *h* current on excitability, as inferred from in vitro analyses, extended to high-conductance neuronal states that are reflective of in vivo synaptic activity.

In addressing these questions, we used a quantitative approach to systematically analyze conductance- and current-based measurements under different combinations of channel configurations and synaptic distributions, with several measures of excitability. Our results from synapse-free models show that the inclusion of KA channels tilts the HCN conductance-current balance heavily in favor of conductance by suppressing the impact of *h* current and enhancing the effects of HCN conductance, thereby resulting in an overall restorative influence on neuronal excitability. On the basis of these results, we postulate the A-type K^+ channel as a candidate mechanism that would fulfill the several requirements of a putative shunting current proposed by (Migliore and Migliore 2012) in enforcing an overall restorative influence on neuronal excitability. In contrast, co-insertion with M-type K^+ channels did not significantly alter either the impact of the HCN conductance or the *h* current consequent to their predominantly perisomatic expression profile and their depolarized activation profile (Chen and Johnston 2004; Hu et al. 2007, 2009; Lewis et al. 2011; Migliore and Migliore 2012; Shah et al. 2008). Finally, when we imposed high-conductance states on the neuronal arbor through synaptic activation, we found that the afferent synaptic drive had a dominant role in defining current- and conductance-based measurements, relegating the conductance-current balance introduced by HCN channels to a subordinate role. Together, our results suggest that HCN channels are not dominant regulators of resting membrane potential (RMP) and excitability under high-conductance states and that they have significant implications for the interaction of HCN channels with other somatodendritic ion channels under physiological and pathophysiological conditions in vivo.

METHODS

We employed morphological reconstructions of rat CA1 pyramidal neurons (*n123* and *ri04*) obtained from http://www.neuromorpho.org (Ascoli et al. 2007; Golding et al. 2005; Pyapali et al. 1998) for our simulations. We imposed biophysical constraints on the passive and active model parameters (Fig. 1*B*) to experimentally match several physiological properties of the model.

Experimental constraints on intrinsic properties of the model neuron. First, we distributed Na^+ ($\bar{g}_{Na}$ = 11 mS/cm^2) and delayed rectifier K^+ (KDR) conductances ($\bar{g}_{KDR}$ = 10 mS/cm^2) with constant density throughout the somatodendritic arbor (Migliore et al. 1999) and ensured unattenuated active propagation of action potentials along the somatoapical trunk (Fig. 1*C*). Next, we set the non-HCN model parameters (Fig. 1, *B–F*) such that *1*) the backpropagating action potential (bAP) amplitude varied from ~100 mV at the soma to ~20 mV at around 300 μm away from the soma when an appropriate KA conductance gradient was inserted; *2*) M-resonance frequency measured at −35 mV was ~4 Hz when M-type K^+ (KM) conductances were distributed perisomatically; and *3*) the input resistance (R_{in}) remained almost constant (~120 MΩ) from the soma to around 300 μm in the apical trunk in the absence of HCN channels (Hoffman et al. 1997; Hu et al. 2007, 2009; Migliore et al. 1999; Narayanan and Johnston 2007). In doing this, we set uniform intracellular resistivity (R_a) at 300 Ω·cm and specific membrane capacitance (C_m) equal to 1 μF/cm^2, and we varied specific membrane resistance, R_m, as a function of radial distance from the soma (x) along the somatoapical trunk (Golding et al. 2005; Narayanan et al. 2010; Narayanan and Johnston 2007; Poirazi et al. 2003; Stuart and Spruston 1998):

$$R_m(x) = R_m^{soma} + \frac{R_m^{end} - R_m^{soma}}{1 + \exp\left[\left(x_d - x\right)/k_{rm}\right]}, \quad (1)$$

where R_m^{soma} = 5.5 kΩ·cm^2 (at soma) and R_m^{end} = 55 kΩ·cm^2 (at terminal trunk location), x_d = 50 μm, and k_{rm} = 10 μm. The KA channel kinetics and voltage dependence properties were different for proximal (<100 μm) and distal apical dendritic regions (Migliore et al. 1999), and their conductance as a function of radial distance from the soma (x) along the somatoapical trunk (Fig. 1*B*) was

$$\bar{g}_{KA}(x) = g_{KA}^{Base}\left(1 + \frac{F_{KA}x}{100}\right), \quad (2)$$

where g_{KA}^{Base} = 2 mS/cm^2 and F_{KA} = 8. The kinetics and voltage-dependent properties of KM channels, distributed perisomatically (≤50 μm), were adopted from (Shah et al. 2008).

Finally, an HCN conductance gradient was inserted on the somatoapical trunk such that R_{in} measured at −65 mV (Fig. 1*B*) varied from ~65 MΩ at the soma to ~20 MΩ at around 300 μm away from the soma (Magee 1998; Narayanan and Johnston 2007):

$$\bar{g}_h(x) = g_h^{Base}\left\{1 + \frac{F_h}{1 + \exp\left[\left(x_h - x\right)/k_h\right]}\right\}, \quad (3)$$

where g_h^{Base} = 100 μS/cm^2, F_h = 100, x_h = 280 μm, and k_h = 34 μm. Kinetics and voltage dependence of HCN channels were adopted from Magee (1998), and the half-maximal activation voltage along the somatoapical axis was −82 mV for $x \leq 100$ μm, varied linearly from −82 to −90 mV for $100 \leq x \leq 300$ μm, and was −90 mV beyond 300 μm (Magee 1998; Poolos et al. 2002). The reversal potentials for K^+ and HCN channels were −90 and −30 mV, respectively. All active and passive basal dendritic parameters were identical to the corresponding somatic parameters, whereas those for apical obliques were equal to corresponding values at the location of their origin on the trunk. This sigmoidal gradient in HCN-channel density (Fig. 1*F*), along with the constraint that the density in apical obliques were equal to the density in their parent trunk compartment, accounted for the experimental observation that the HCN-channel density in the stratum lacunosum moleculare dendrites is similar to that in the distal dendrites of the stratum radiatum (Bittner et al. 2012). These channel properties together also ensured (Fig. 1*G*) that the two complementary forms of resonance mediated by HCN and KM channels (Hu et al. 2002, 2009) were observed at different voltage ranges, and they matched with experimental ranges (Lewis et al. 2011; Narayanan and Johnston 2007) and prior sensitivity analyses of the interactions between HCN and KA channels (Rathour and Narayanan 2012a, 2014). Together, imposing these constraints ensured that the functional maps regulated by the HCN, KA, and KM channels were accounted for in our model (Narayanan and Johnston 2012).

Unless otherwise mentioned, the passive and active properties mentioned above are the default values employed in our simulations. The temperature dependence of the kinetics and/or conductance of each channel was accounted for by using Q_{10} factors obtained through

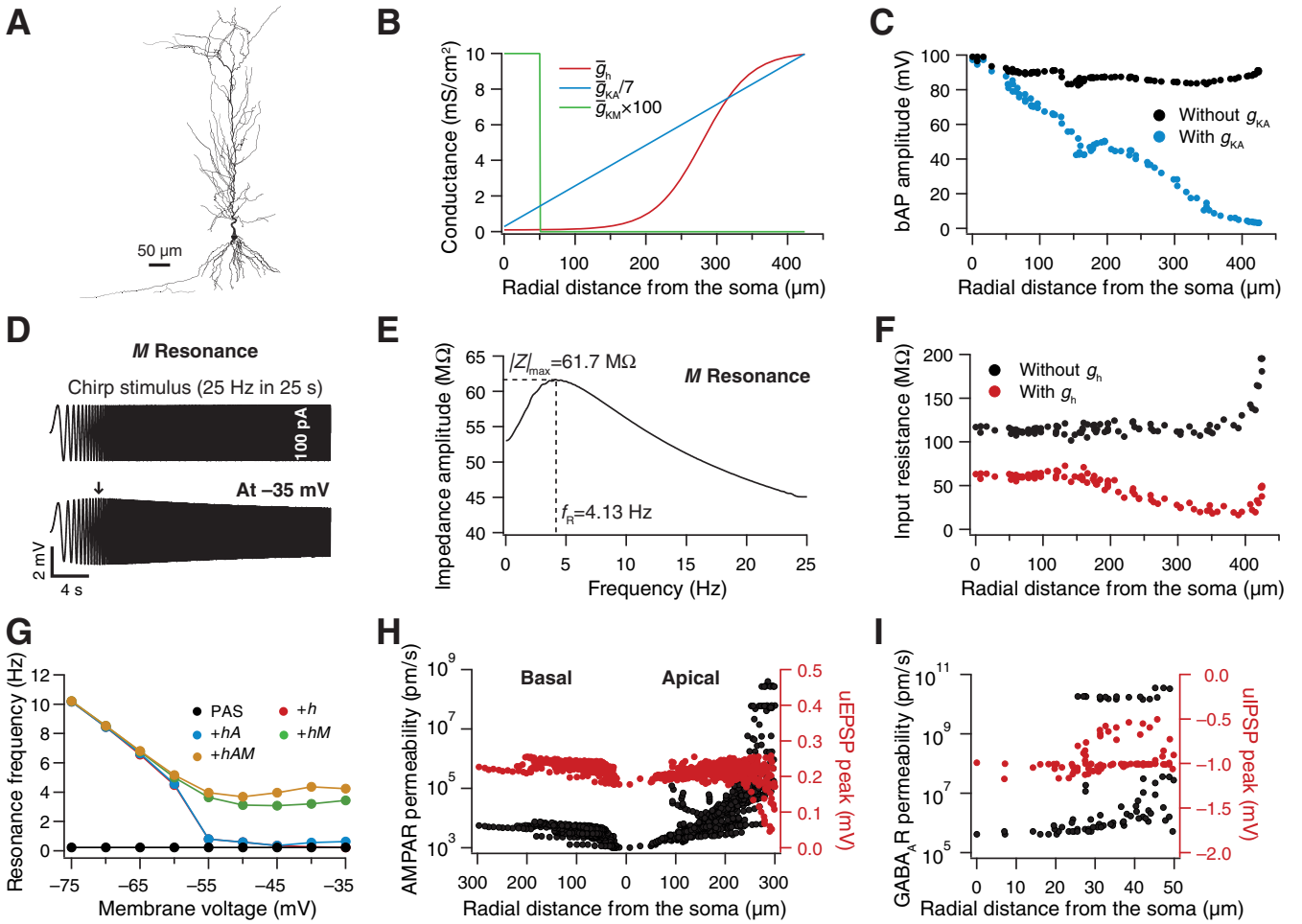

Fig. 1. Experimental constraints on the intrinsic and synaptic properties of a morphologically realistic CA1 pyramidal model neuron. *A*: 2-dimensional projection of a 3-dimensional reconstructed hippocampal CA1 pyramidal neuron model. *B*: experimentally constrained somatodendritic distributions of the hyperpolarization-activated cyclic nucleotide-gated (HCN; $\bar{g}_h$), A-type K^+ (KA; $\bar{g}_{KA}$), and M-type K^+ (KM; $\bar{g}_{KM}$) channels, to match physiological measurements in *C*–*F*. *C*: backpropagating action potential (bAP) amplitude plotted as a function of radial distance from the soma (μm), in the presence and absence of KA channels, with HCN and KM channels included as shown in *B*. When present, $\bar{g}_{KA}$ was distributed as shown in *B*. *D*: a chirp stimulus of 100-pA amplitude with frequency linearly spanning 0–25 Hz in 25 s (*top*) and the corresponding somatic voltage response measured at −35 mV (*bottom*), employed to characterize and constrain M resonance. *E*: impedance amplitude profile obtained from traces shown in *D*. *F*: input resistance (R_{in}) plotted as a function of radial distance from the soma, in the presence and absence of HCN channels, with KA and KM channels included as shown in *B*. When present, $\bar{g}_h$ was distributed as shown in *B*. *G*: resonance frequency plotted as function of membrane voltage for a passive model (PAS) and for models with the independent or co-insertion of HCN channels (+*h*) with other channels (+*hA*, +*hM*, +*hAM*, were *A* and *M* represent the KA and KM channels, respectively). *H* and *I*: location-dependent permeability values of AMPA receptor (AMPAR; *H*) and $GABA_A$ receptor ($GABA_AR$; *I*) that normalized somatic unitary excitatory postsynaptic potential (uEPSP) amplitudes to around 0.2 mV (*H*) and somatic unitary inhibitory postsynaptic potential (uIPSP) amplitudes to around −1 mV (*I*).

experiments (Magee 1998; Migliore et al. 1999; Poolos et al. 2002; Shah et al. 2008).

Experimental constraints on excitatory and inhibitory model synapses. The excitatory and inhibitory synapses comprised AMPA and $GABA_A$ receptors, respectively. Independent random spike generators, with each firing at an average rate of 8 Hz, were used as inputs to these synapses. The choice of 8 Hz was consequent to the strong theta modulation of inputs to CA1 pyramidal neurons (Buzsáki 2002). The AMPA receptor current, as a function of voltage (v) and time (t), was modeled as (Narayanan and Johnston 2010)

$$I_{AMPA}(v,t) = I^{Na}_{AMPA}(v,t) + I^{K}_{AMPA}(v,t), \tag{4}$$

where

$$I^{Na}_{AMPA}(v,t) = \bar{P}_{AMPA} P_{Na} s(t) \frac{vF^2}{RT} \left\{ \frac{[Na]_i - [Na]_o \exp(-vF/RT)}{1 - \exp[-vF/RT]} \right\} \tag{5}$$

and

$$I^{K}_{AMPA}(v,t) = \bar{P}_{AMPA} P_K s(t) \frac{vF^2}{RT} \left\{ \frac{[K]_i - [K]_o \exp(-vF/RT)}{1 - \exp(-vF/RT)} \right\}, \tag{6}$$

where F was Faraday's constant, R depicted gas constant, T was temperature, and $\bar{P}_{AMPA}$ was the maximum permeability of AMPA receptor. $s(t)$ governed the AMPA receptor kinetics and was set as follows:

$$s(t) = a\left[\exp(-t/\tau_d) - \exp(-t/\tau_r)\right], \tag{7}$$

where a normalized $s(t)$ such that $0 \le s(t) \le 1$, τ_d (= 10 ms) represented the decay time constant, and τ_r (= 2 ms) depicted the rise time. P_{Na} was equal to P_K. Internal and external ionic concentrations used for *Eqs. 5* and *6* were as follows: $[Na]_i$ = 18 mM, $[Na]_o$ = 140 mM, $[K]_i$ = 140 mM, and $[K]_o$ = 5 mM, which established the reversal potentials for sodium and potassium ions at +55 and −90 mV, respectively. We confirmed the reversal potential for AMPA receptor as ~0 mV. Variable numbers of excitatory synapses were

distributed randomly across somatodendritic compartments within 300-μm radial distance from the soma. $\bar{P}_{\mathrm{AMPA}}$ was calculated for each dendritic compartment such that a synapse at any location was constrained by the experimental finding that the somatic unitary excitatory postsynaptic potential (uEPSP) was ~0.2 mV (Fig. 1*H*), irrespective of the dendritic location of the synapse (Magee and Cook 2000; Narayanan and Chattarji 2010).

The $\mathrm{GABA_A}$ receptor current, as a function of voltage and time, was modeled as a chloride current:

$$I^{CL}_{GABAA}(v,t) = \bar{P}_{GABAA}s(t)\frac{vF^2}{RT}\left\{\frac{\left[Cl\right]_i - \left[Cl\right]_o\exp\left(-vF/RT\right)}{1-\exp\left(-vF/RT\right)}\right\}, \quad (8)$$

where $\bar{P}_{\mathrm{GABAA}}$ was the maximum permeability of $\mathrm{GABA_A}$ receptor. $s(t)$ was identical to that for AMPA receptor. $[\mathrm{Cl}]_\mathrm{i}$ = 5 mM and $[\mathrm{Cl}]_\mathrm{o}$ = 98 mM, setting the reversal potential for $\mathrm{GABA_A}$ receptors at −80 mV. Inhibitory synapses were distributed randomly across compartments within 50 μm of radial distance from the soma (Megias et al. 2001). $\bar{P}_{\mathrm{GABAA}}$ was calculated for each perisomatic compartment such that an inhibitory synapse at that location elicited a somatic unitary inhibitory postsynaptic potential (uIPSP) of around −1.0 mV (Buhl et al. 1994), independent of synapse location (Fig. 1*I*).

Periodic synaptic stimulation. Several combinations of excitatory and inhibitory synapses (with different total numbers of synapses) were distributed across the somatodendritic arbor, with the relative number of each type set to achieve balanced excitation-inhibition at around −65 mV. Spike timings of incoming inputs were Gaussian modulated for both excitatory and inhibitory inputs, with a standard deviation set at one-eighth and one-fifth of the oscillatory cycle, respectively. The inhibitory inputs were set to have a 60° phase lead with reference to the excitatory inputs (Csicsvari et al. 1999; Klausberger et al. 2003; Klausberger and Somogyi 2008). Specifically, the number of action potentials received by an excitatory synapse was governed by the distribution (Schomburg et al. 2012)

$$N_e(t) = A_e\exp\left\{-\frac{\left[\mathrm{mod}(t,T) - T/2\right]^2}{2\sigma_e^2}\right\}, \quad (9)$$

and those received by an inhibitory synapse were governed by

$$N_i(t) = A_i\exp\left\{-\frac{\left[\mathrm{mod}(t+\psi,T) - T/2\right]^2}{2\sigma_i^2}\right\}, \quad (10)$$

where T represents the time period of the oscillations, $\sigma_\mathrm{e} = T/8$, $\sigma_\mathrm{i} = T/5$, mod represents the modulo function, and ψ in $N_\mathrm{i}(t)$ constitutes the 60° phase lead in inhibitory synaptic inputs. Although all excitatory and inhibitory synapses followed their respective distributions above, individual synaptic timings were independent and randomized with this constraint on the distribution.

Computational details and measurements. All simulations were performed using the NEURON simulation environment (Carnevale and Hines 2006) at 34°C with an integration time step of 25 μs. Compartmentalization of the model neuron was performed such that the length of each compartment was less than 10% of the corresponding space constant computed at 100 Hz (Carnevale and Hines 2006). Simulations with high background activity were repeated for several trials, with trials differing from each other in terms of *1*) the distribution of excitatory and/or inhibitory synapses across these compartments and *2*) the pattern of synaptic stimulation they receive. Simulations performed across different channel configurations (e.g., PAS vs. +*h*) were trial matched, implying that the same synaptic locations with the same stimulation patterns were employed for a given trial so that a direct comparison of the results (across channel configurations) from a specific trial was made possible. The trial average for a given channel configuration was computed as the mean of voltage responses obtained across different trials with that channel configuration. For all simulations, conductance densities, when the corresponding channels were included as part of the simulations, were set as depicted in Fig. 1*B*.

For a passive model, the RMP was set at −70 mV across the somatodendritic arbor. For simulations performed in the absence of any synaptic stimulation (e.g., Fig. 2), RMP at different dendritic compartments reflected the presence of ionic conductances active at rest and was measured (e.g., Fig. 2, *B* and *C*) after the evolution achieved steady state (300 ms after the start of the simulation). R_in values for these simulations (e.g., Fig. 2*E*) were measured at this steady-state RMP of the neuron (300 ms after the start of the simulation) by using a long current pulse (amplitude, 100 pA; duration, 700 ms) that would allow the membrane potential response to this pulse to settle at its steady-state value. The steady-state deflection in the voltage response was divided by the current amplitude to compute R_in. This procedure ensured that the RMP was determined by the temporal evolution of the different conductances present on the neuronal membrane, thereby setting the simulation methodology to be as close to physiology as possible. For instance, blocking HCN channels through ZD7288 hyperpolarizes the RMP of soma and dendrites of hippocampal pyramidal neurons (Gasparini and DiFrancesco 1997; Magee 1998) and constitutes the impact of the inward *h* current on neuronal physiology (see Fig. 2).

For simulations performed with background synaptic activity, RMP was measured as the time average across a 50-ms period (450–500 ms after the evolution began) on a trial-averaged trace (default n = 10 trials), where the 450-ms measurement delay was to achieve steady-state conditions of the ionic currents active at rest. A depolarizing current pulse was injected for 500 ms, after an initial 500-ms delay to ensure that the average RMP reached steady state, for measuring R_in at the RMP. The current-pulse amplitude was 100 pA, except for simulations performed with balanced excitation-inhibition, where it was 500 pA, due to large background fluctuations. In this case, the "steady-state" deflection in the voltage response was measured as the time average across a 50-ms period (450–500 ms after the current-pulse onset) on a trial-averaged trace. This average value of steady-state voltage deflection was divided by the current amplitude to compute R_in.

The average percent change in RMP across two channel configurations (e.g., Fig. 3*D*, PAS and +*hAM*) was computed as

$$\text{Average } \%\Delta RMP = \sum_{i=1}^{N_{Trial}}\frac{RMP_i^{PAS} - RMP_i^{hAM}}{RMP_i^{PAS}} \times 100, \quad (11)$$

where $\mathrm{RMP}_i^{\mathrm{PAS}}$ and RMP_i^{hAM} represent the RMP computed from the *i*-th trial in a passive model neuron and in a neuron where all channels (HCN, KA, and KM) were incorporated, respectively. These trial-matched differences were possible because the simulations with the same trial number across channel configurations had the same synaptic configurations and stimulation patterns. Within-trial fluctuations in membrane potential were analyzed by quantifying the standard deviation (SD) of the voltage values measured during the trial, and the across-trial mean of these SD values was plotted as a measure of synaptically driven fluctuations. The average percentage of changes in R_in and in peak-to-peak voltage (PPV; for rhythmic stimulation) was computed using a similar procedure. All data analyses were performed with custom-written software made using the IGOR Pro (WaveMetrics) programming language.

The peak conductance-voltage (*g-V*) curves for activation and inactivation of the Hodgkin-Huxley (HH)-type KA channel models (Fig. 2*A*) were plotted directly from the steady-state values of the corresponding gating variables (Hoffman et al. 1997; Migliore et al. 1999). The *g-V* curves for activation and inactivation for the multistate Markovian models (both CSI and CSI-OSI) were obtained with appropriate voltage-clamp protocols (Hodgkin and Huxley 1952) on a compartment where these channels were incorporated. Specifically, for obtaining the activation *g-V*, the compartment was allowed to rest at −160 mV, and a voltage-pulse of various amplitudes (taking the

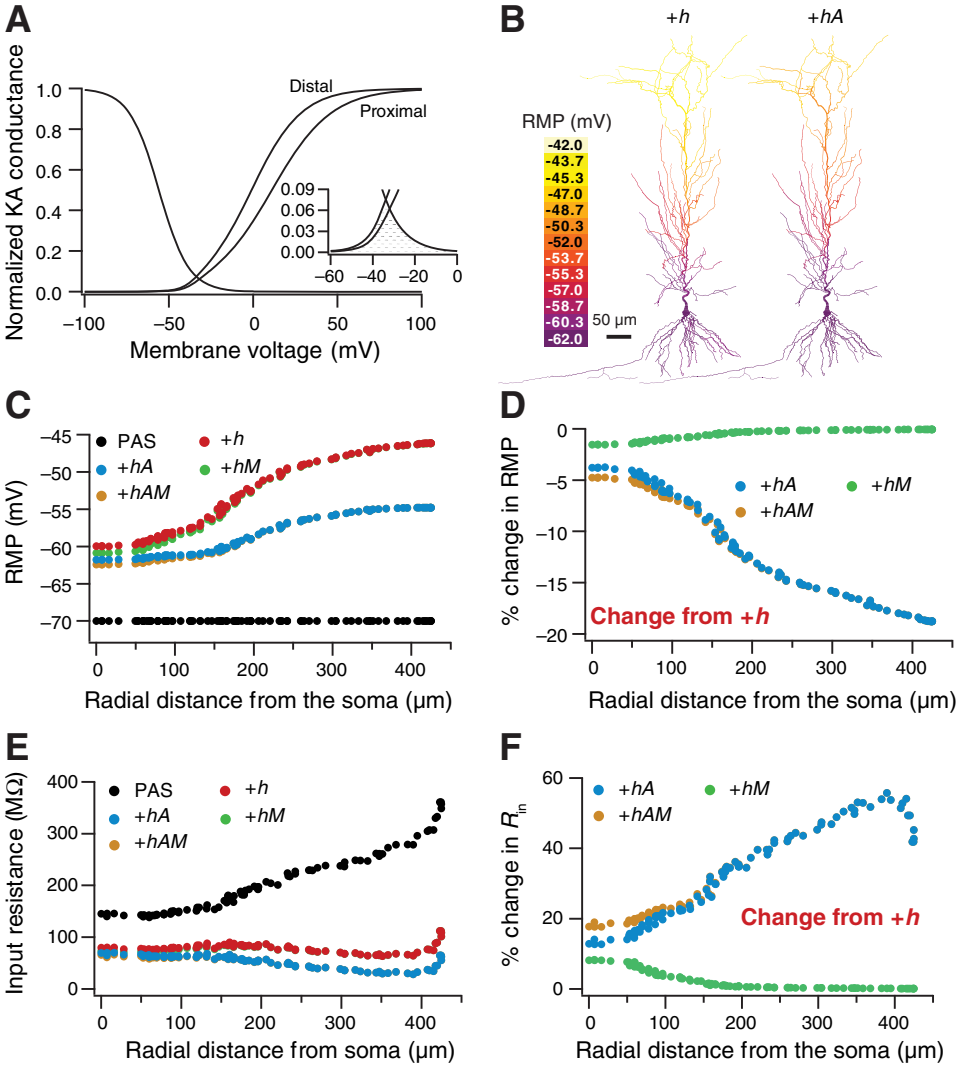

Fig. 2. Co-insertion with KA channels altered the efficacy of current- and conductance-based changes introduced by HCN channels. *A*: voltage-dependent activation and inactivation profiles of KA channels in proximal and distal dendritic regions of CA1 pyramidal neurons. Note the significant window component in both the proximal and the distal A currents (*inset* depicts a zoomed version, with the window component shaded). *B*: heat map of resting membrane potential (RMP) overlaid on a neuronal reconstruction in the absence (+*h*) and presence (+*hA*) of KA channels. HCN channels were already present. *C*: RMP plotted as a function of radial distance along the somatoapical trunk plotted for a passive model (PAS) and for models with the independent or co-insertion of HCN channels (+*h*) with other channels (+*hA*, +*hM*, +*hAM*). *D*: percent change in RMP from +*h* condition for 3 combinations, +*hA*, +*hM*, and +*hAM*, obtained from data used for plotting *C*, depicting the impact of co-insertion of other channels with HCN channels. *E*: R_{in} plotted as a function of radial distance along the somatoapical trunk for the 5 channel configurations shown in *C*. *F*: percent change in R_{in} from +*h* condition for channel configurations shown in *D*.

compartment to voltage values ranging from −150 to +150 mV) was applied for 500 ms. The peak conductance achieved during the pulse period was measured and was plotted as a function of the pulse-voltage amplitude to get the activation *g-V*. For obtaining the inactivation *g-V*, a two-pulse protocol was followed whereby the compartment was taken to several voltage levels (−150 to +150 mV) using a long prepulse of 700 ms and then switched to +250 mV using a second pulse of 250 ms. The peak conductance achieved during the second pulse period was then plotted as a function of the prepulse voltage amplitude to get the inactivation *g-V*.

RESULTS

We employed R_{in} and RMP as direct measures of conductance and current changes consequent to the inclusion of HCN channels, respectively, and assessed them under different configurations of synaptic and/or voltage-gated ionic conductances. We first used these measurements to analyze the impact of other ion channels on HCN-channel function in a synapse-free model and then subsequently explored models under different configurations of synaptic inputs.

Co-insertion of HCN channels with KA channels tilts the conductance-current balance in favor of conductance. Because HCN channels are predominantly expressed in the dendrites of hippocampal and cortical pyramids, we asked if the impact of their presence could be altered by the additional incorporation of KA channels. To do this, we co-inserted HCN channels with KA channels and/or M-type K^+ (KM) channel, a perisomatic channel that has been implicated in altering HCN-channel function upon coexpression (George et al. 2009), and compared RMP and R_{in} under these channel configurations with those in either a passive structure or in the sole presence of HCN channels.

Upon independent insertion of HCN channels, the RMP depolarized from its passive value of −70 mV, with a larger shift in dendritic locations than at the soma (Fig. 2, *B* and *C*). This was to be expected as a direct consequence of higher density of HCN channels in the dendrite (Fig. 1*B*). Strikingly, upon co-insertion with KA channels (as in Fig. 1*B*), the depolarizing shift in RMP was significantly reduced (Fig. 2, *B* and *D*). Importantly, given the predominant dendritic presence of KA channels, this reduction was higher at the dendritic locations, implying a pronounced reduction in the somatodendritic difference in RMP (cf. +*h* vs. +*hA*, Fig. 2, *B* and *D*). In contrast, co-insertion of HCN channels with KM channels did not result in significant changes to the dendritic RMP, with a small difference in somatic RMP (Fig. 2, *C* and *D*). This was a direct outcome of the perisomatic presence and depolarized activation voltages of KM channel (Chen and Johnston 2004;

Shah et al. 2008). When we included all three channels together, we found the somatodendritic RMP profile to be very similar to that obtained with only the HCN and KA channels (Fig. 2, *B* and *C*), implying a large contribution of KA channels to the (dendritic) RMP.

We measured R_{in} to assess conductance changes and found that the independent inclusion of HCN channels elicited a large reduction in R_{in} (compared with the passive model), with larger changes observed in the dendrites (Fig. 2, *E* and *F*). Upon co-insertion of KA channels with HCN channels, we found R_{in} to further reduce from the model where only HCN channels were present. This was a consequence of KA channels contributing to the resting conductance, given that the corresponding RMP (Fig. 2*C*) fell within the window component of the A-current (Fig. 2*A*). It should be noted that the RMP was within the A-current window as a direct consequence of the presence of HCN channels, without which the RMP was hyperpolarized to the window (Fig. 2*A*). Finally, we found the contribution of KM channels to R_{in} to be very minimal even at perisomatic regions (Fig. 2, *E* and *F*). Together, these results suggest that co-insertion with KA, but not KM, channels partially negated the impact of *h* current on the RMP while amplifying the impact of HCN conductance on R_{in}, thereby tilting the overall balance in favor of conductance.

High-conductance states tempered the efficacy of current- and conductance-based changes triggered by HCN channels. Analyses of HCN channel-induced conductance-current balance have been confined to in vitro physiology, where afferent activity to a neuron is sparse. However, under in vivo conditions, a neuron receives inputs through several thousands of synapses, which control the average resting potential and gain of the neuron. How do high-conductance neuronal states alter the conductance-current balance induced by HCN channels? To address this, we introduced several excitatory or inhibitory synapses randomly across the somatodendritic arbor, and stimulated them with randomized inputs (see METHODS). Because of the minimal independent influence of KM channels (Fig. 2), we chose the three significantly different configurations (passive, PAS; independent insertion of HCN, $+h$; and co-insertion of HCN, KA, and KM channels, $+hAM$) for further analyses under high-conductance states. To assess the independent contributions of excitatory and inhibitory synapses on our measurements, we first analyzed high-conductance states achieved solely through excitatory or inhibitory synapses (Fig. 3).

As expected, stimulation of inhibitory synapses to achieve high background activity in a passive neuron hyperpolarized the RMP and reduced R_{in} (Fig. 3, *A* and *C*). Although these effects of imposing background inhibitory activity were qualitatively similar across different channel configurations, there were important quantitative differences that shed light on the HCN conductance-current balance. Specifically, an increase in the number of active inhibitory synapses significantly diminished the difference in the average RMP between a passive model and a model where HCN channels were included (Fig. 3, *A*, *B*, and *D*). Similarly, the impact of HCN conductance on R_{in} was significantly reduced with increasing number of inhibitory synapses contributing to the high-conductance state (Fig. 3, *A*, *C*, and *D*). These conclusions extended to the model where all three channels were present (Fig. 3, *A–D*). The SD of somatic voltage fluctuations reduced with an increase in number of inhibitory synapses and was lowest in the passive neuron (Fig. 3*E*), as direct consequences of the lower driving force when RMP was closer to the inhibitory synaptic reversal potential (Fig. 3*B*). When we effectuated a high-conductance state through activation of excitatory synapses, we observed a depolarizing shift to the RMP, accompanied by a reduction in R_{in}, spanning all tested channel configurations (Fig. 3, *F–H*). Again, upon comparing RMP and R_{in} in a passive neuron with those in neurons with HCN channels, we found that increasing numbers of excitatory synapses significantly diminished the impact of both the *h* current and conductance on both measurements (Fig. 3, *F–H*).

A prominent difference between achieving the high-conductance state through excitatory vs. inhibitory synapses was the role of KA channels, which had a significant impact on RMP and R_{in} if excitatory (Fig. 3, *F–H*), but not inhibitory (Fig. 3, *B–D*), synapses were activated. This is to be expected because the average RMP with excitatory synapses (Fig. 3*F*) was within the activation range of KA channels (Fig. 2*A*), but with inhibitory synapses, the average RMP was more hyperpolarized, thereby eliciting no KA-channel activation (Fig. 3*B*). Furthermore, with an increasing number of excitatory synapses and consequent depolarization of average RMP, the membrane voltage was beyond the activation range of HCN channels, implying a lesser contribution of HCN channels to RMP and R_{in} under an excitatory (but not inhibitory) high-conductance state (Fig. 3, *F–H*). Together, these results suggested that aperiodic high-conductance states achieved solely through excitatory or through inhibitory synapses significantly reduced the impact of HCN channels on RMP and R_{in}, suggesting a domination of synaptic conductances in regulating these measurements.

High-conductance states with balanced excitation-inhibition tempered the efficacy of current- and conductance-based changes triggered by HCN channels. Next, to avoid these voltage-dependent influences on somatic measurements (Fig. 3) and to achieve physiologically important balance in excitation-inhibition, we inserted various combinations of excitatory and inhibitory synapses such that the average somatic voltage was -65 mV when all three channels were included in the model (Table 1). Although we had tuned the number of synapses to achieve somatic balance in the presence of all three channels, the somatic balance of excitation-inhibition was invariant to the channel configuration when we employed the same synaptic numbers and distributions (Fig. 4, *A* and *B*). This meant that the RMP was predominantly regulated by the synaptic drive, and the role of *h* current was insignificant. However, a small difference in RMP (Fig. 4, *B* and *D*) was noted with the additional inclusion of KA channels, due to dendritic depolarization (below), but the difference was significantly diminished when larger numbers of synapses were activated. The differences in R_{in} across the three channel configurations was very minimal, with the difference reaching zero even with ~1,000 synapses activated (Fig. 4, *C* and *D*). In summary, the differences in RMP and R_{in} imposed by the HCN channels in a synapse-free in vitro-like model (Fig. 2) were reduced by in vivo-like high-conductance states (Figs. 3 and 4), where synaptic currents and conductances played dominant roles in driving RMP and R_{in}. The SD of somatic voltage fluctuations exhibited a small reduction with increase in total synapse number (Fig. 4*E*) consequent to the reduction in the driving force of excitatory synapses (Fig. 4, *F–H*). Assessing

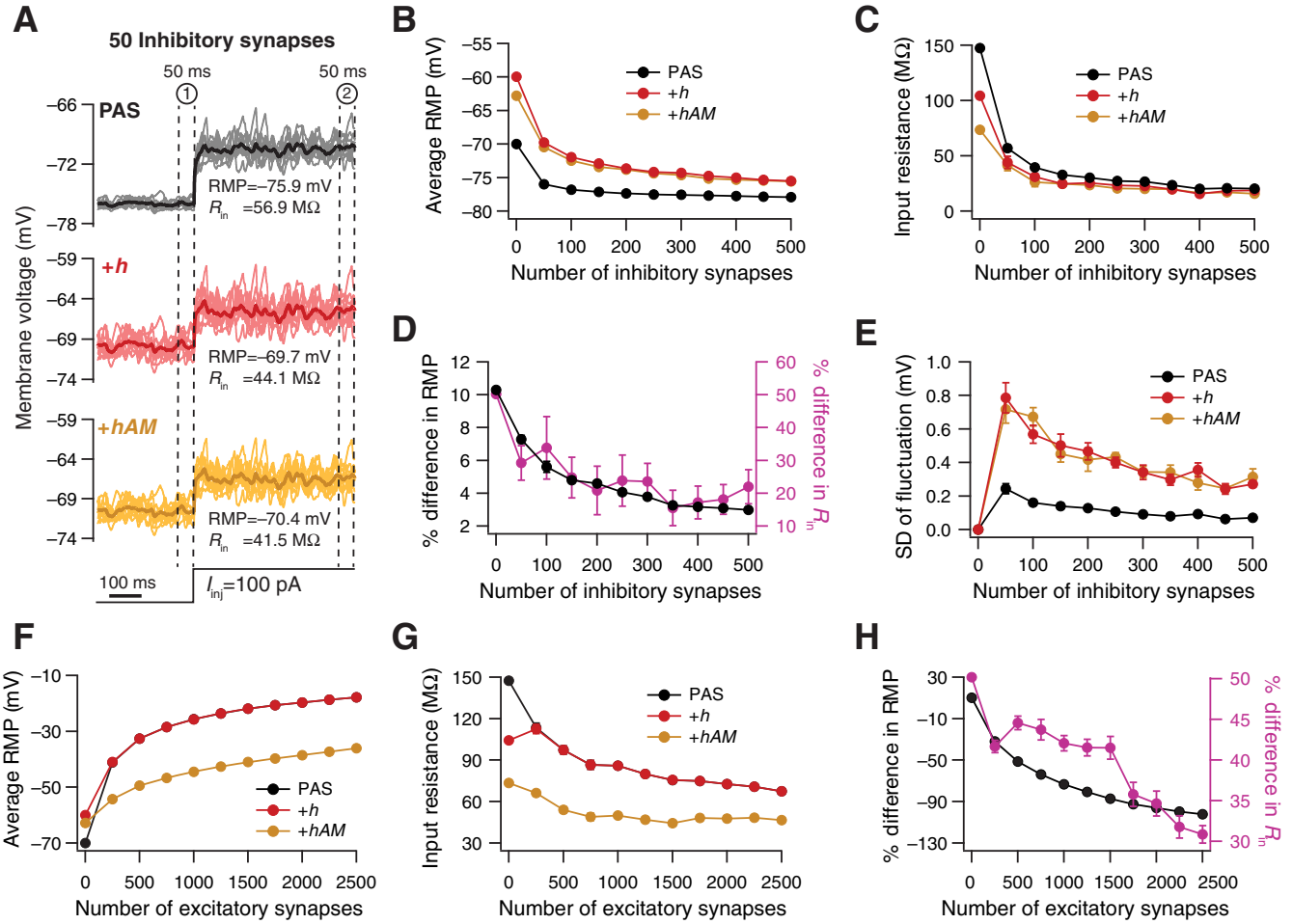

Fig. 3. High-conductance state, achieved through inhibitory or excitatory synaptic bombardment, tempered the efficacy of current- and conductance-based changes introduced by HCN channels. *A*: voltage traces recorded from the soma through different trials (n = 10; thin traces) and their average (thick trace), obtained in response to a current pulse of 100-pA amplitude injected after a 500-ms delay. The traces depict 300 ms before and 500 ms after the onset of the current pulse for a passive neuronal model (PAS) and independent and co-insertion of HCN channels (+*h*) with the KA and KM channels (+*hAM*). Random synaptic bombardments from 50 inhibitory synapses were afferent to the neuron through the course of these simulations. *B* and *C*: average RMP (*B*) and R_{in} (*C*) plotted as functions of number of inhibitory synapses for different channel configurations (*A*). The average RMP and the "steady-state" voltage deflection (for computing R_{in}) in response to a 100-pA current pulse were computed by time-averaging the trial-averaged voltage traces over the 50-ms period marked by *areas 1* and *2* in *A*, respectively. *D*: percent differences in RMP and R_{in} plotted as functions of number of inhibitory synapses. Differences were computed between the PAS and +*hAM* configurations. The error bars (SE) depict the across-trial variability in the computed RMP and R_{in} values. *E*: average (across-trial) standard deviation (SD) of within-trial fluctuations plotted as a function of number of inhibitory synapses for different channel configurations. The error bars (SE) depict the across-trial variability in the within-trial SD. *F–H*: same as *B–D*, but with high-conductance state achieved through excitatory synapses. Data in *B–H* are means ± SE and depict variability across trials.

voltage fluctuations under the different synaptic and channel configurations (Figs. 3*E* and 4*E*), we noted that the spread (SD) of voltage fluctuations could be considered as an additional measure of excitability. Specifically, the larger the range of fluctuations from −65 mV, the larger is the probability that the cell fires an action potential and therefore the higher is the excitability. This also may be observed from the qualitative similarity between the average R_{in} and the SD of fluctuations measured across synaptic configurations (Figs. 3 and 4), both of which reduced with an increase in number of synaptic inputs.

Finally, given the predominant dendritic presence of KA and HCN channels, we assessed the role of these channels in altering dendritic RMP under balanced somatic RMP. We found that the dendritic average resting voltages were much depolarized with reference to the balanced (−65 mV) somatic voltages (Fig. 4, *F* and *G*) consequent to the predominant placement of excitatory and inhibitory synapses at dendritic and perisomatic locations, respectively. Therefore, under the influence of a large excitatory synaptic drive, dendritic HCN channels were completely closed by the depolarization. On the other hand, KA channels played a critical role in regulating dendritic RMP (Fig. 4*G*; cf. Fig. 2*C*), thereby steering synaptic driving forces toward differential modulation of fluctuations at different locations (Fig. 4*H*). Together, these results suggested that aperiodic high-conductance states, achieved through synapses imposing balanced excitation-inhibition on the cell body, significantly reduced the impact of HCN channels on RMP and R_{in}, suggesting a domination of synaptic conductances in regulating these measurements.

The regulation of HCN channel physiology by KA channels and high-conductance states was invariant to changes in axial resistivity. How dependent are our conclusions on the specific choice of parameters? To address this question, we first re-

Table 1. *Combinations of excitatory and inhibitory synapses (for Fig. 4) required for balancing the average somatic membrane potential at −65 mV in the presence of HCN, KA, and KM channels*

No. of Excitatory Synapses	No. of Inhibitory Synapses	Total No. of Synapses
1,090	110	1,200
2,200	200	2,400
3,325	275	3,600
4,475	325	4,800
5,625	375	6,000
6,780	420	7,200
7,940	460	8,400
9,115	485	9,600
10,275	525	10,800
11,425	575	12,000

HCN, hyperpolarization-activated cyclic nucleotide-gated channel; KA, A-type K^+ channel; KM, M-type K^+ channel.

peated our experiments (Figs. 2 and 4) with axial resistivity (R_a) to two values different from the default 300 Ω·cm (Fig. 5). Because changes in R_a translate to altered intrinsic properties, it was necessary *1*) to alter other parameters to constrain the several coexistent functional maps by their physiological counterparts (as in Fig. 1, *B–F*), and *2*) to retune location-dependent excitatory and inhibitory permeability values so that the synaptic inputs would yield ~0.2- and ~1-mV somatic postsynaptic potentials, respectively (as in Fig. 1, *H* and *I*). We effectuated this by changing the active and passive properties of the neuronal model for every change in the value of R_a (Fig. 5, *A* and *B*) and by retuning permeability values for each of these combinations.

After ensuring that physiological constraints were imposed on models with different values of R_a, we first tested the impact of different ion channel configurations on RMP and R_{in} in the absence of any synaptic input. Consistent with our earlier results with the default value of R_a, we found that the co-insertion of HCN channels with KA channels tilted the conductance-current balance in favor of conductance for both tested values of R_a (Fig. 5, *C–F*). Specifically, whereas there was a distance-dependent depolarization in the RMP across the trunk upon independent insertion of HCN channels, this depolarization was partially suppressed upon co-insertion of the KA channels (Fig. 5, *C* and *D*). This reduction was higher at dendritic locations, implying a pronounced reduction in the somatodendritic difference in RMP upon co-insertion of HCN channels with KA channels. Furthermore, independent insertion of HCN channels elicited a large reduction in R_{in} (compared with the passive model), and a further reduction in R_{in} was observed with the co-insertion of KA channels with HCN channels. This reduction in R_{in} was more pronounced in the distal dendritic locations where these channels are present at higher densities.

Next, we turned to how the impact of high-conductance state on HCN-channel physiology would be altered under various values of R_a. We bombarded the neuronal model, equipped with different ion channel combinations, with incrementally higher numbers of synapses such that excitatory-inhibitory balance was retained (as in Fig. 4). We then asked if the evolution of RMP and R_{in} as functions of synaptic number was robust to changes in R_a by plotting the percent change in both these measurements under various channel configurations (Fig. 5, *G* and *H*). We found our results, obtained with different values of R_a (Fig. 5, *G* and *H*), to be consistent with our earlier conclusions that high-conductance states with balanced excitation-inhibition tempered the efficacy of current- and conductance-based changes triggered by HCN-channel insertion (cf. Fig. 4*D*). Together, these results indicate that our conclusions on the ability of KA channels and high-conductance states to regulate the HCN conductance-*h* current balance were robust to variability in R_a and consequent changes in other active and passive properties.

The regulation of HCN channel physiology by KA channels and high-conductance states was robust to changes in synaptic distribution. Although we considered inhibition to be perisomatic thus far, it is well established that inhibitory synapses do make contact on dendrites, as well (Klausberger and Somogyi 2008; Megias et al. 2001). How dependent are our conclusions on the specific distribution of inhibitory synapses across the dendritic arbor? To address this question, we repeated our experiments (Fig. 4) with two different distributions of inhibitory synapses: one where 60% of inhibitory synapses were perisomatic and the remaining 40% on distal dendrites (60P-40D distribution), and the second where these percentages were reversed (40P-60D distribution; Fig. 6). For either case, we independently found incrementally larger combinations of excitatory and inhibitory synapses to achieve balanced excitation-inhibition at the soma. We used such balanced inputs to assess the impact of co-inserting various channel combinations on R_{in} and RMP under high-conductance states (Fig. 6, *A–F*). We found that the conclusions, using both 60P-40D and 40P-60D combinations, were consistent with our previous results using perisomatic inhibition alone (Fig. 6, *A–F*; cf. Fig. 4, *B–D*). Specifically, with an increase in the overall synapse number, the differences in RMP and R_{in} imposed by the HCN channels in a synapse-free model (Figs. 2 and 5, *C–F*) were reduced by high-conductance states realized through several combinations of synaptic distributions (Figs. 4–6).

With an altered somatodendritic inhibitory profile, would there be a change in the somatodendritic RMP in the presence of the synaptic barrage? To address this question, we recorded somatodendritic RMP under conditions of balanced somatic RMP with several channel combinations (as in Fig. 4*G*). Consistent with Fig. 4*G*, we found that the average dendritic resting voltages were much depolarized with reference to the balanced (−65 mV) somatic voltages (Fig. 6, *G* and *H*). However, given the presence of larger dendritic inhibition, dendritic RMP values obtained with the 40P-60D distribution (Fig. 6*H*; peak RMP: PAS, −29.4 mV; +*h*, −29.4 mV; +*hAM*, −30.7 mV) were more hyperpolarized than those with 60P-40D distribution (Fig. 6*G*; peak RMP: PAS, −23.0 mV; +*h*, −23.0 mV; +*hAM*, −24.4 mV), which in turn were more hyperpolarized than the perisomatic inhibition case (Fig. 4*G*; peak RMP: PAS, −2.9 mV; +*h*, −2.9 mV; +*hAM*, −4.4 mV). Therefore, and as expected, the relative locations and activation profiles of synaptic excitation and inhibition determine the exact somatodendritic voltage profiles, and KA channels play a critical role in regulating dendritic RMP (Fig. 6, *G* and *H*, Fig. 4*G*; cf. Fig. 2*C*). Together, our results from Figs. 3–6 suggest that the presence of high-conductance states, irrespective of the mode of their realization, tempered the impact of current- and conductance-based changes triggered by the presence of HCN channels.

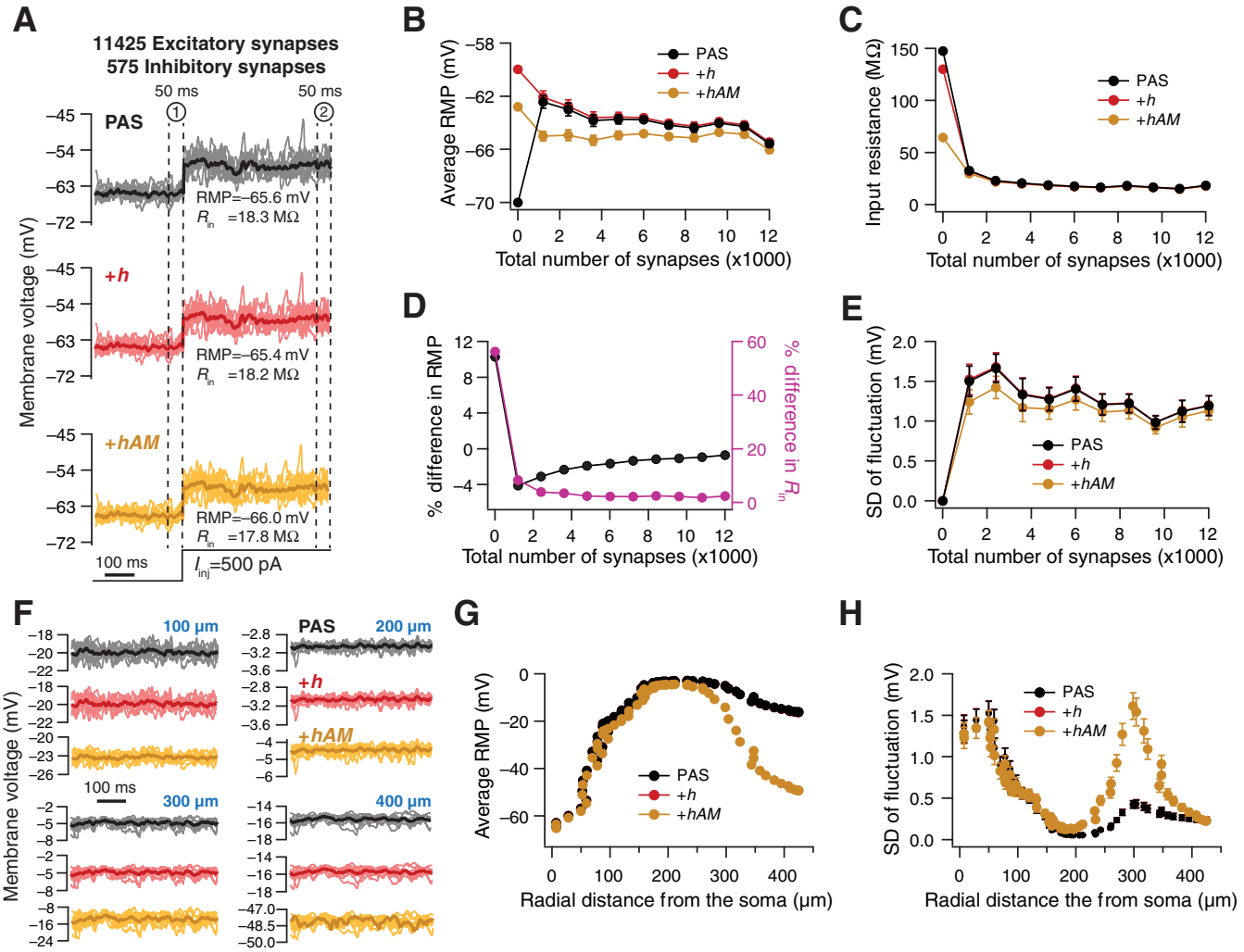

Fig. 4. High-conductance state, achieved under balanced excitatory and inhibitory synaptic bombardment, tempered the efficacy of current- and conductance-based changes introduced by HCN channels. *A*: same as Fig. 3*A*, but with balanced excitation-inhibition achieved through random synaptic bombardment from 11,425 excitatory synapses and 575 inhibitory synapses distributed across the somatodendritic arbor. *B* and *C*: average RMP (*B*) and R_{in} (*C*) plotted as functions of total (excitatory + inhibitory) number of synapses for different channel configurations (*A*). The average RMP and the "steady-state" voltage deflection (for computing R_{in}) in response to a 500-pA current pulse (I_{inj}) were computed by time-averaging the trial-averaged voltage traces over the 50-ms period marked by *areas 1* and *2* in *A*, respectively. *D*: percent differences in RMP and R_{in} plotted as functions of total number of synapses. Differences were computed between the PAS and +*hAM* configurations. The error bars (SE) depict the across-trial variability in the computed RMP and R_{in}. *E*: average (across-trial) SD of within-trial fluctuations plotted as a function of total number of synapses for different channel configurations. The error bars (SE) depict the across-trial variability in the within-trial SD. *F*: voltage traces recorded from 4 different apical trunk locations through different trials (n = 10; thin traces) and their average (thick trace), obtained with balanced excitation-inhibition (as observed at the soma). The traces depict the last 500 ms of 1,000-ms simulations used to achieve "steady-state" of the balance for different channel configurations. *G* and *H*: average RMP and SD of fluctuation plotted as a function of radial distance from the soma for different channel configurations and with 12,000 total synapses. Note the overlap between the PAS and +*h* plots in *G* and *H*.

The regulation of HCN conductance-current balance by KA channels and high-conductance state was manifest in the presence of spike-generating conductances. Thus far, we had looked at subthreshold measures of neuronal physiology, considering RMP as a measure of the impact of the inward *h* current and R_{in} as a measure of gain that would reflect the change in the HCN conductance. How does this balance manifest under conditions where the neuron fires action potentials? How does the additional presence of KA channels or high-conductance state alter firing rate, a well-established measure of excitability? To address these questions, we inserted spike-generating conductances into the neuronal membrane with their default distributions and conductance values (see METHODS) and assessed both subthreshold and firing rate properties of the model neuron (Fig. 7). Note that the channel combinations mentioned here (Fig. 7) are in addition to the presence of spike-generating conductances and are distinguished from those in other figures by the addition of +NaK to the labels.

First, we asked if the insertion of spike-generating conductances altered the subthreshold properties and their dependencies on the insertion of ionic conductances in various combinations. Because the independent insertion of HCN channels or its co-insertion with only the KM channels resulted in a large depolarization to the RMP, the neuron sustained spontaneous firing, thereby precluding the measurement of RMP and R_{in} at RMP under these channel combinations (Fig. 7*A*; +*h*+NaK and +*hM*+NaK). Importantly, and further emphasizing our earlier observations, the neuron ceased to fire spontaneously when KA channels, but not KM channels, were co-inserted

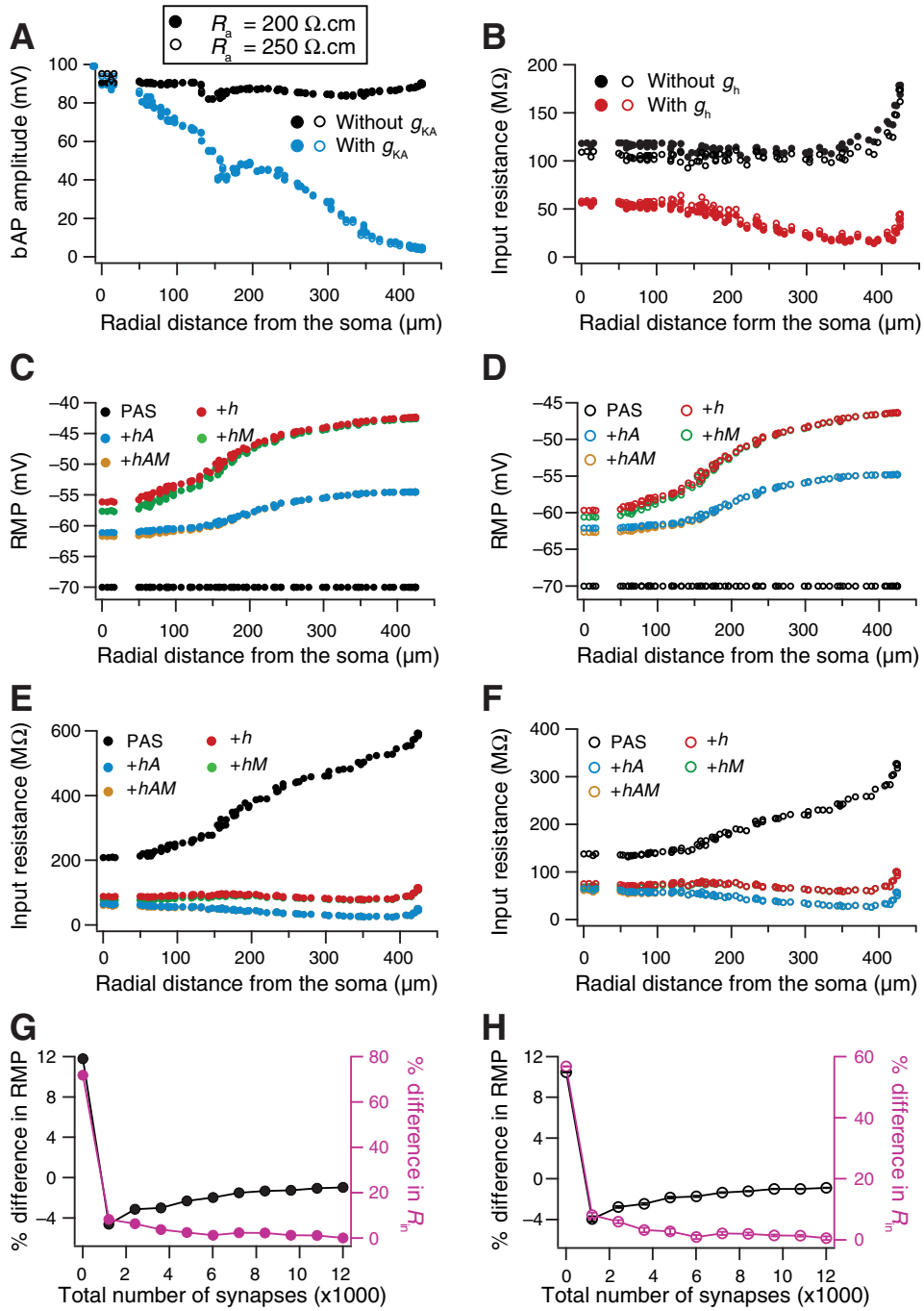

Fig. 5. Sensitivity analyses with various values of axial resistivity (R_a) confirmed the roles of KA channels and high-conductance states in regulating HCN channel-induced conductance-current balance. Across all panels, filled and open circles represent plots for R_a = 200 Ω·cm and R_a = 250 Ω·cm, respectively. For R_a = 250 Ω·cm, R_m^{soma} = 5.5 kΩ·cm^2, R_m^{end} = 55 kΩ·cm^2, x_d =50 μm, and k_{rm} =10 μm and for R_a=200 Ω·cm, R_m^{soma} = 30 kΩ·cm^2, R_m^{end} = 400 kΩ·cm^2, x_d = 10 μm, and k_{rm} = 100 μm. The synaptic permeabilities were recomputed for each value of R_a such that the uEPSP and uIPSP values were ~0.2 and ~1 mV, respectively, irrespective of synapse location. *A*: bAP amplitude plotted as a function of radial distance from the soma, in the presence and absence of KA channels, computed in the presence of HCN and KM channels. *B*: R_{in} plotted as a function of radial distance from the soma, in presence and absence of HCN channels, computed with KA and KM channels included. *C* and *D*: RMP plotted as a function of radial distance along the somatoapical trunk for a passive model (PAS) and for models with the independent or co-insertion of HCN channels (+*h*) with other channels (+*hA*, +*hM*, +*hAM*) for R_a = 200 Ω·cm (*C*) and R_a = 250 Ω·cm (*D*). *E* and *F*: R_{in} plotted as a function of radial distance along the somatoapical trunk for the 5 channel configurations shown in *C* for R_a = 200 Ω·cm (*E*) and R_a = 250 Ω·cm (*F*). *G* and *H*: percent differences in RMP and R_{in} plotted as functions of total number of synapses for R_a = 200 Ω·cm (*G*), and R_a = 250 Ω·cm (*H*). Differences were computed between the PAS and +*hAM* configurations.

with HCN channels, implying that co-insertion of KA channels significantly suppresses the impact of the inward *h* current on neuronal physiology. The co-insertion of KA channels further reduced R_{in} (Figs. 2*E* and 7*B*) in addition to the reduction brought about by the insertion of HCN channels, implying that the impact of HCN conductance was enhanced by the co-insertion of KA channels. It also may be noted that the RMP and R_{in} values for channel combinations where the neuron did not spontaneously fire, including the passive case, were nearly identical to the case where the spike-generating conductances were absent (compare Fig. 7*A* with Fig. 2*C* and Fig. 7*B* with Fig. 2*E*). Together, these results imply that, in the absence of synaptic inputs, co-insertion of KA channels tilts the HCN conductance-current balance heavily in favor of conductance, and this tilt translated to significant changes in firing frequency in the presence of spike-generating conductances.

How does the presence of HCN channels alter firing patterns under high-conductance states? What impact does the co-insertion of KA and KM channels have on these firing patterns? To address these questions, we presented balanced synaptic stimulation with increasing numbers of synapses in the presence of spike-generating conductances. As mentioned above, in the absence of any synaptic input, the model containing only the spike-generating conductances (PAS+NaK) and the model co-inserted with all HCN, KA and KM (+*hAM*+NaK) channels did not fire spontaneously, but the one with independent co-insertion of HCN channels (+*h*+NaK) fired spontaneously (Fig. 7, *C* and *D*). With increase in number of

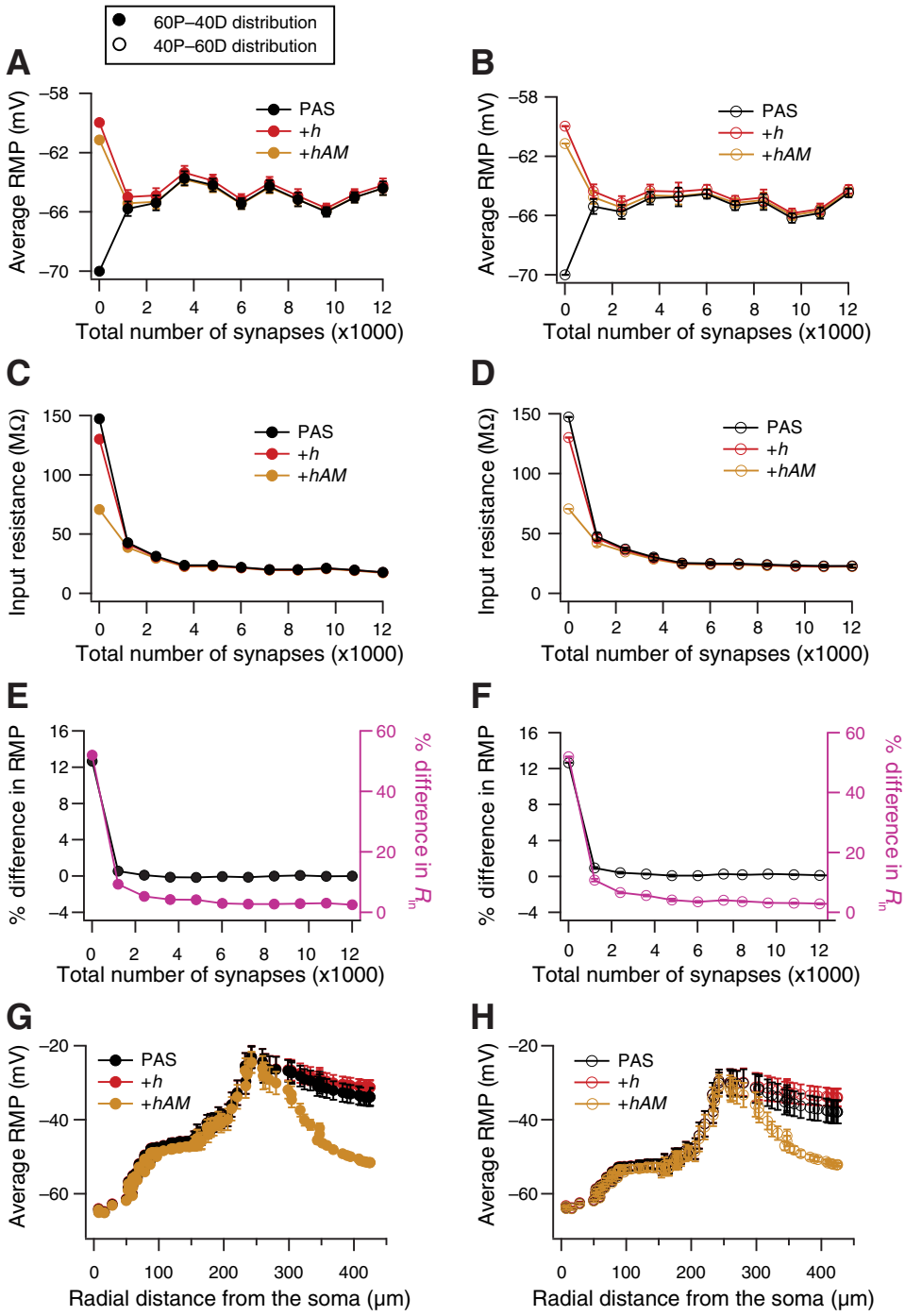

Fig. 6. High-conductance state achieved with different distributions of inhibitory synapses along somatodendritic axis tempered the efficacy of current- and conductance-based changes introduced by HCN channels. Across panels, filled circles represent plots for the case where 60% of inhibitory synapses were perisomatically distributed (≤50 μm) and 40% were located in more distal locations (>50 μm), referred to as 60P-40D, and open circles represent plots for the synaptic distribution where percentages were reversed between the perisomatic and distal locations, referred to as 40P-60D. The synaptic permeabilities were recomputed such that the uIPSP value was ~1 mV irrespective of location. *A* and *B*: average RMP plotted as a function of total (excitatory + inhibitory) number of synapses for the 60P-40D (*A*) and 40P-60D distributions (*B*) for different channel configurations. *C* and *D*: average R_{in} plotted as a function of total number of synapses for the 60P-40D (*C*) and 40P-60D distributions (*D*) for different channel configurations. *E* and *F*: percentage differences in RMP and R_{in} plotted as functions of total number of synapses for the 60P-40D (*E*) and 40P-60D distributions (*F*). Differences were computed between the PAS and +*hAM* configurations. *G* and *H*: average RMP plotted as a function of radial distance from the soma, computed for different channel configurations and with 12,000 total synapses, for the 60P-40D (*G*) and 40P-60D distributions (*H*). Note the overlap between the PAS and +*h* plots in *G* and *H*. Data are means ± SE.

synapses enforcing balanced excitation-inhibition, the neuronal firing rate expectedly increased (Fig. 7, *C* and *D*), due to the larger SD in membrane potential fluctuation (Fig. 4*E*). However, the firing rates attained with identical synaptic stimulation were highest for the case where only HCN channels were present (+*h*+NaK) and lowest for the case where HCN channels were included along with KA and KM (+*hAM*+NaK) channels (Fig. 7, *C* and *D*). Whereas the former observation was a direct consequence of the depolarized membrane potential in the independent presence of HCN channels (Fig. 7*A*), the latter is to be expected as a consequence of the KA-induced tilt yielding a significant reduction in R_{in} apart from hyperpolarizing the membrane (Fig. 7, *A* and *B*).

With a further increase in the number of synapses, due to the consequent dendritic depolarization and the shutdown of HCN channels, the firing rates for the PAS+NaK and the +*h*+NaK cases were nearly identical. However, the firing rates associated with the +*hAM*+NaK case were always lower than those achieved with both PAS+NaK and +*h*+NaK cases (Fig. 7*D*). When we further increased the number of synapses beyond a certain threshold on the number of synapses, the neurons ceased firing. This threshold was nearly identical for the PAS+NaK and the +*h*+NaK cases but was lower for the +*hAM*+NaK case (Fig. 7, *C* and *D*). We inferred this to be a direct consequence of the reduction in R_{in} with increase in number of synapses, with the +*hAM*+NaK case showing the

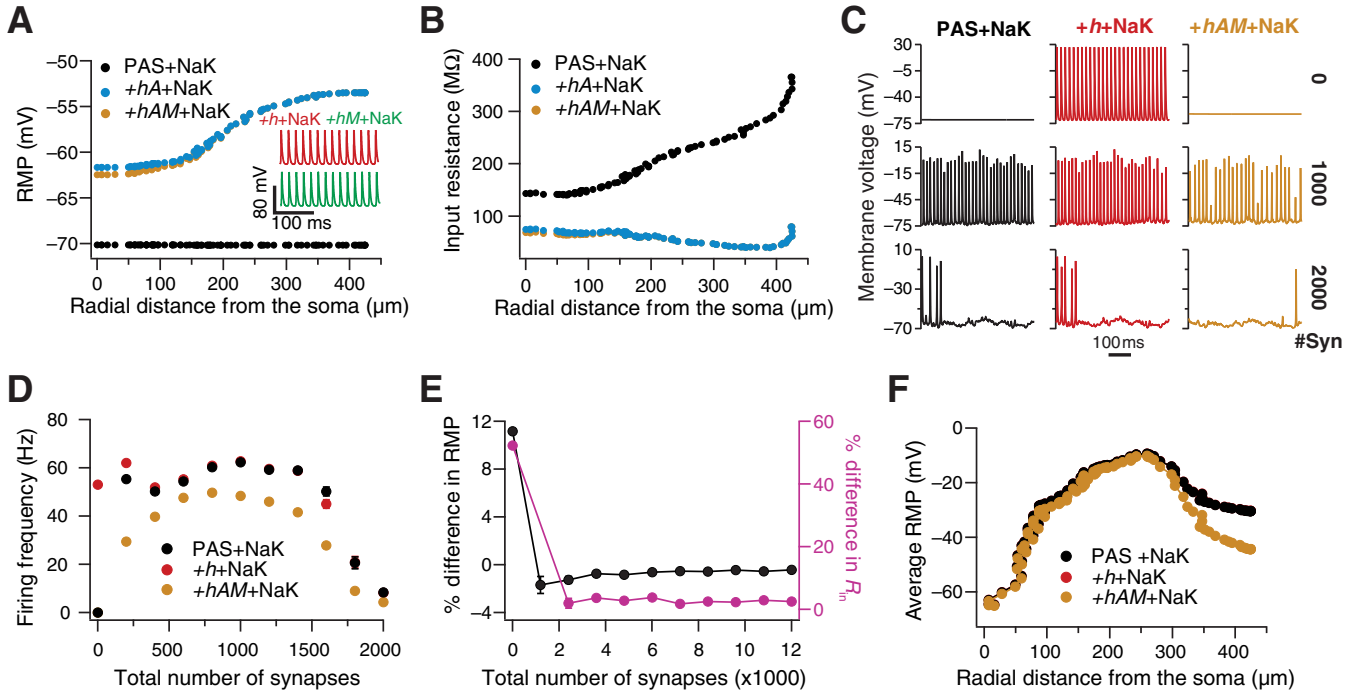

Fig. 7. KA channels and high-conductance state regulated the efficacy of current- and conductance-based changes introduced by HCN channels in the presence of spike-generating conductances. "+NaK" indicates the presence of spike-generating Na^+ and delayed rectifier K^+ (KDR) conductances. *A*: RMP plotted as a function of radial distance along the somatoapical trunk plotted for a passive model (PAS+NaK) and for models with the co-insertion of HCN channels (+*h*+NaK) with other channels (+*hA*+NaK, +*hAM*+NaK). *Inset* depicts spontaneous firing in neuronal models with independent and co-insertion of HCN channels (+*h*+NaK) with only the KM channel (+*hM*+NaK). *B*: R_{in} plotted as a function of radial distance along the somatoapical trunk for the 3 channel configurations shown in *A*. *C*: membrane voltage dynamics of models endowed with different channel configurations plotted in the presence of different numbers of synapses (0, 1,000, and 2,000 synapses). *D*: action potential firing frequency plotted as a function of total number of synapses for different channel configurations. *E*: percent differences in RMP and R_{in} plotted as functions of total number of synapses. Differences were computed between the PAS+NaK and +*hAM*+NaK channel configurations. *F*: average RMP plotted as a function of radial distance from the soma for different channel configurations. Note the overlap between the PAS+NaK and +*h*+NaK plots. For *C*–*F*, the synaptic permeabilities were recomputed such that the uEPSP and uIPSP values were ~0.2 and ~1 mV, respectively, irrespective of synapse location.

least R_{in} with all synaptic configurations (Fig. 7*B*; also see Fig. 4*C*). From these analyses on action potential firing, it was clear that co-insertion with KA channels suppressed the impact of the inward *h* current and enhanced the influence of the HCN conductance, together resulting in an overall reduction in neuronal excitability.

When the total number of synapses was taken beyond ~2,000 (Fig. 7*E*), neurons failed to fire action potentials because of the low R_{in} (Fig. 4*C*) and reduced fluctuations (Fig. 4*E*). Consequently, we were able to measure both RMP and R_{in} for these synaptic configurations by using the methodology outlined in Fig. 4*A*. Consistent with our previous observations (Fig. 4*D*, Fig. 5, *G* and *H*, Fig. 6, *E* and *F*), we found that with increase in number of synapses (in the range between 2,000 and 12,000), the synaptic currents and conductances played dominant roles in driving RMP and R_{in}, and the impact of HCN channels on R_{in} was severely weakened under such high-conductance states. Finally, we computed the average RMP along the somatodendritic trunk with 12,000 total synapses and found that dendritic depolarization still existed, but with lower peak values (Fig. 7*F*; cf. Fig. 4*G*) due to the additional activation of KDR channels. We also noted that dendritic Na channels would be inactivated at such depolarized voltages, and their slow kinetics for recovery from inactivation would ensure that they remained nonconducting.

Together, in this set of results, we employed action potential firing as a measure of excitability to validate our previous conclusions (with R_{in} as the measure of excitability; Figs. 2–6) that KA channels and high-conductance states were potent regulators of the balance between the restorative influence of HCN conductances and the regenerative influence of the *h* current.

HCN conductance-current balance was regulated by KA channels modeled as multistate kinetic schemes in the presence and absence of balanced synaptic stimulation. In the simulations for all the results presented above, we had employed HH-type models (Hodgkin and Huxley 1952) for hippocampal KA channels. How dependent were our conclusions on this choice of model type? How would our conclusions change if we employed a multistate Markovian kinetic model for the KA channels? To address this question, we employed two different kinetic models for KA channels (Amarillo et al. 2008; Fineberg et al. 2012), the first of which sustained only closed-state inactivation (CSI; Fig. 8*A*) and the other endowed with state transitions that enabled both open-state and closed-state inactivation (CSI-OSI; Fig. 9*A*). It should be noted that the *g*-*V* curves for activation and inactivation of the CSI (Fig. 8*B*) and CSI-OSI models (Fig. 9*B*) show a significantly diminished window component compared with hippocampal KA channels shown in Fig. 2*A* [compare Amarillo et al. (2008) and Fineberg et al. (2012) with Hoffman et al. (1997) and Migliore et al. (1999)]. In replacing the HH-type KA channels with either the CSI or the CSI-OSI Markov models, as in earlier cases, we ensured that the physiological measure-

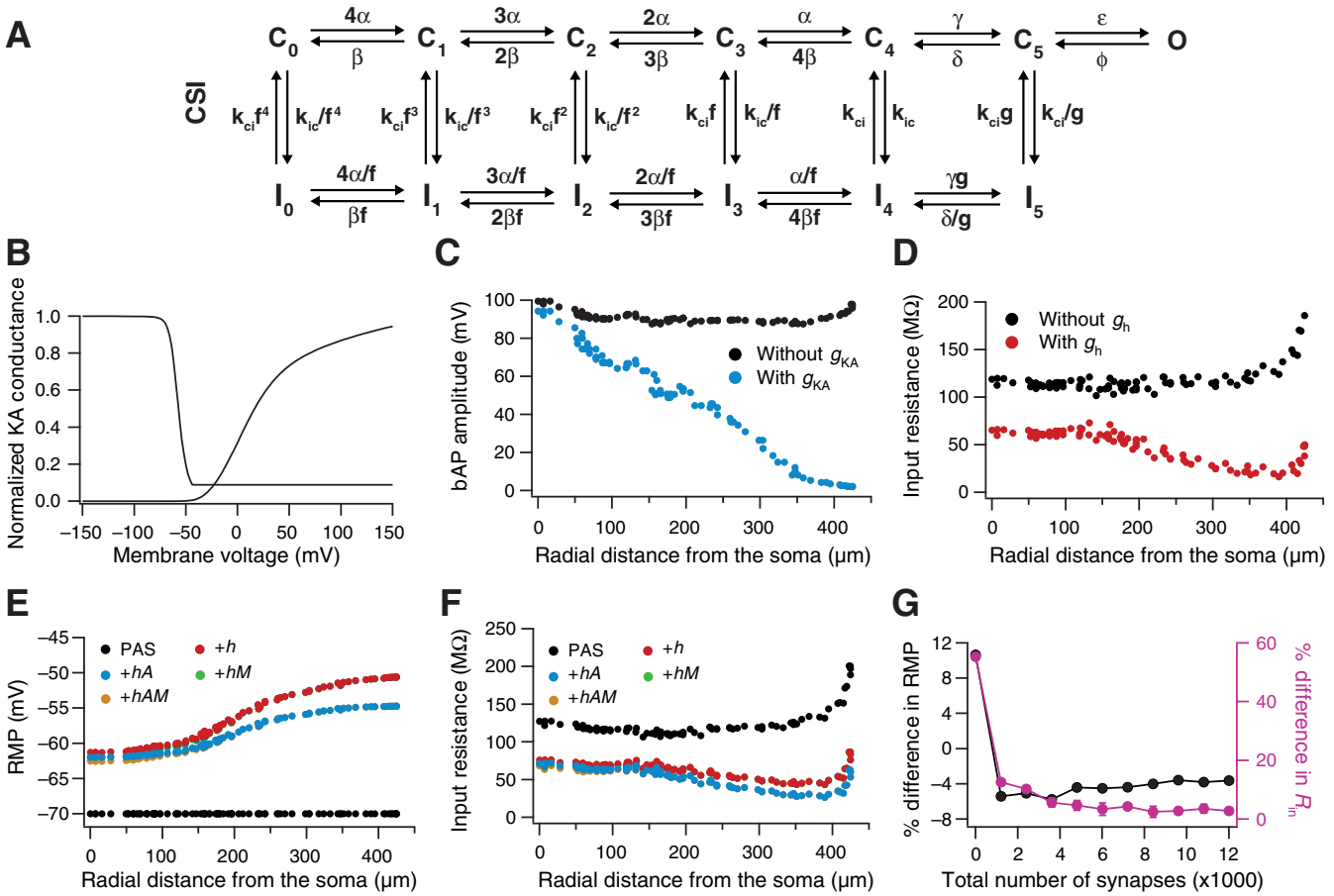

Fig. 8. KA channels modeled with a multistate kinetic scheme endowed with closed-state inactivation (CSI) regulated the HCN conductance-current balance in the presence and the absence of synaptic inputs. Parametric values were g_{KA}^{Base} = 35 mS/cm^2, F_{KA} = 5, $\bar{g}_{Na}$ = 26 mS/cm^2, $\bar{g}_{KDR}$ = 190 mS/cm^2, R_m^{soma} = 32 kΩ·cm^2, R_m^{end} = 16 kΩ·cm^2, x_d = 150 μm, and k_{rm} =10 μm. *A*: kinetic scheme representing the CSI Markov model of the KA channel (Amarillo et al. 2008; Fineberg et al. 2012). *B*: voltage-dependent activation and inactivation profiles of CSI KA channels. *C*: bAP amplitude plotted as a function of radial distance from the soma, in the presence and absence of CSI KA channels, with HCN and KM channels incorporated as in Fig. 1*B*. *D*: R_{in} plotted as a function of radial distance from the soma, in the presence and absence of HCN channels, with KA and KM channels included. In matching these base measurements with their experimental counterparts, the value of g_{KA}^{base} was larger and membrane resistance (R_m) displayed an inverse gradient, compared with the case where we had used the Hodgkin-Huxley (HH) model for KA channels (*Eq. 1*). We noted these and the other associated parametric changes (mentioned above) as a consequence of the smaller window component in the CSI Markov model (*B*) compared with that in the HH model (Fig. 2*A*). *E* and *F*: RMP (*E*) and R_{in} (*F*) plotted as functions of radial distance along the somatoapical trunk for different channel configurations. *G*: percent differences in RMP and R_{in} plotted as functions of total number of synapses when the model was subjected to balanced excitation-inhibition. Differences were computed between the PAS and +*hAM* configurations. Synaptic permeabilities were recomputed such that the uEPSP and uIPSP values were ~0.2 and ~1 mV, respectively, irrespective of synapse location.

ments of the model were constrained from experimental data. Specifically, we first adjusted the passive and active properties such that the gradients in bAP amplitude (CSI, Fig. 8*C*; CSI-OSI, Fig. 9*C*) and R_{in} (CSI, Fig. 8*D*; CSI-OSI, Fig. 9*D*) were accounted for.

After establishing the base physiological maps with these multistate KA channel models, we first asked if these channels regulated RMP and R_{in} in a manner that was similar to the HH models employed earlier (Fig. 2,*C–F*, Fig. 5,*C–F*, Fig. 7, *A* and *B*). To do this, we obtained both measurements in the absence of synaptic inputs under various channel configurations with KA channels realized with either the CSI (Fig. 8, *E* and *F*) or the CSI-OSI model (Fig. 9, *E* and *F*). These results were consistent with our earlier conclusions, establishing that the co-insertion of KA channels suppresses the impact of the *h* current in depolarizing the RMP (CSI, Fig. 8*E*; CSI-OSI, Fig. 9*E*) and reduces R_{in} (CSI, Fig. 8*F*; CSI-OSI, Fig. 9*F*) beyond the reduction imposed by the presence of HCN channels. Next, to understand the impact of interactions between high-conductance states and the multistate KA channel models in regulating the HCN conductance-current balance, we retuned location-dependent excitatory and inhibitory permeability values so that the synaptic inputs would yield ~0.2- and ~1-mV unitary somatic potentials, respectively (as in Fig. 1, *H* and *I*). We then activated these synapses through incrementally larger numbers of balanced excitatory-inhibitory inputs and estimated the average R_{in} and RMP values for each synaptic configuration, using either CSI and CSI-OSI KA channels. We found, with either kinetic model for KA channels, that the differences in RMP and R_{in} imposed by HCN channels in the synapse-free models (CSI, Fig. 8, *E* and *F*; CSI-OSI, Fig. 9, *E* and *F*) were significantly suppressed with an increase in total number of synapses. Under these high-conductance states, synaptic currents and conductances played dominant roles in driving both RMP and R_{in} (CSI, Fig. 8*G*; CSI-OSI, Fig. 9*G*). Together, these results (Figs. 8–9) validated our previous conclusions (obtained with HH KA channels in Figs. 2–6) with multistate Markovian KA channels.

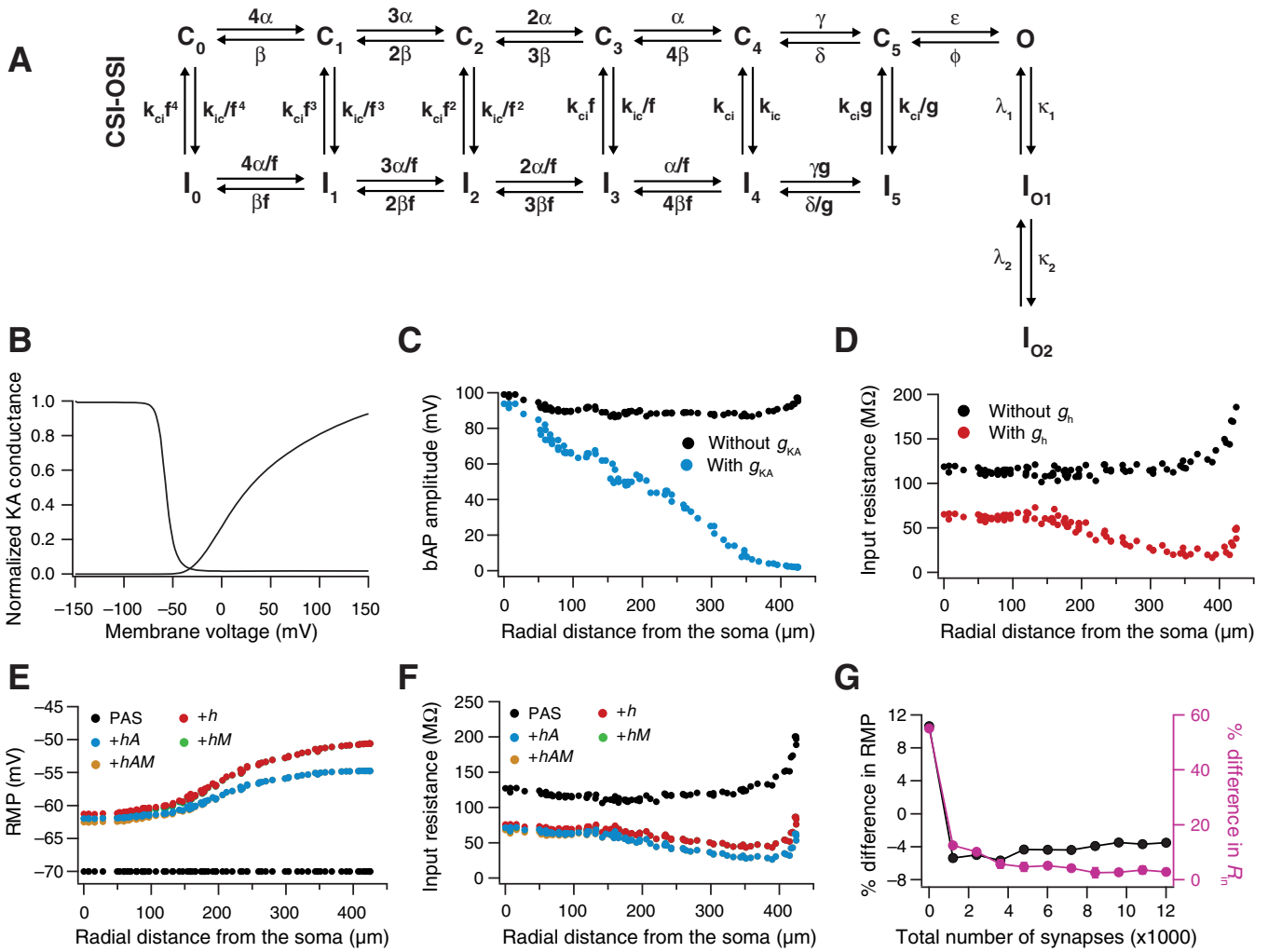

Fig. 9. KA channels modeled with a multistate kinetic scheme endowed with both closed- and open-state inactivation (CSI-OSI) regulated the HCN conductance-current balance in the presence and the absence of synaptic inputs. Parametric values were g_{KA}^{Base} = 35 mS/cm^2, F_{KA} = 5, $\bar{g}_{Na}$ = 25 mS/cm^2, $\bar{g}_{KDR}$ = 190 mS/cm^2, R_m^{soma} = 32 kΩ·cm^2, R_m^{end} = 16 kΩ·cm^2, x_d = 150 μm, and k_{rm} = 10 μm. *A*: kinetic scheme representing the CSI-OSI Markov model of the KA channel (Amarillo et al. 2008; Fineberg et al. 2012). *B*: voltage-dependent activation and inactivation profiles of CSI-OSI KA channels. *C*: bAP amplitude plotted as a function of radial distance from the soma, in the presence and absence of CSI-OSI KA channels, with HCN and KM channels incorporated as in Fig. 1*B*. *D*: R_{in} plotted as a function of radial distance from the soma, in the presence and absence of HCN channels, with KA and KM channels included. In matching these base measurements with their experimental counterparts, the value of g_{KA}^{base} was larger and R_m displayed an inverse gradient, compared with the case where we had used the HH model for KA channels (*Eq. 1*). We noted these and the other associated parametric changes (mentioned above) as a consequence of the smaller window component in the CSI-OSI Markov model (*B*) compared with that in the HH model (Fig. 2*A*). *E* and *F*: RMP (*E*) and R_{in} (*F*) plotted as functions of radial distance along the somatoapical trunk for different channel configurations. *G*: percent differences in RMP and R_{in} plotted as functions of total number of synapses when the model was subjected to balanced excitation-inhibition. Differences were computed between the PAS and +*hAM* configurations. Synaptic permeabilities were recomputed such that the uEPSP and uIPSP values were ~0.2 and ~1 mV, respectively, irrespective of synapse location.

The regulation of HCN conductance-current balance by rhythmic high-conductance state was dependent on the oscillatory frequency and on KA channels. In our simulations thus far, we had employed aperiodic synaptic stimulation to achieve high-conductance states. However, in the hippocampus and in several other brain regions, afferent synaptic inputs are modulated by an oscillatory frequency (Buzsáki 2006, 2002; Schomburg et al. 2012; Wang 2010), thereby eliciting membrane potential oscillations at that particular frequency (Domnisoru et al. 2013; Harvey et al. 2009; Schmidt-Hieber and Hausser 2013). Are our conclusions valid under rhythmic high-conductance states? To test this, we first chose 8-Hz theta-frequency modulations of afferent inputs (Fig. 10*A*) because of the predominant presence of theta modulation in the hippocampal subregion (Buzsáki 2006, 2002; Schomburg et al. 2012; Wang 2010). We modulated the spatiotemporally distributed excitatory and inhibitory inputs by 8-Hz oscillatory patterns (see METHODS), which expectedly resulted in 8-Hz membrane potential oscillations under different channel combinations (Fig. 10*A*). The average RMP was designed to be approximately −65 mV across all synaptic numbers when all three channels (+*hAM*) were co-inserted by balancing the numbers of excitatory and inhibitory inputs in each synaptic configuration. However, when we assessed average RMP for the other channel configurations, we found a depolarization in the membrane potential as the consequence of the nonuniform spatial distribution of these channels and the fact

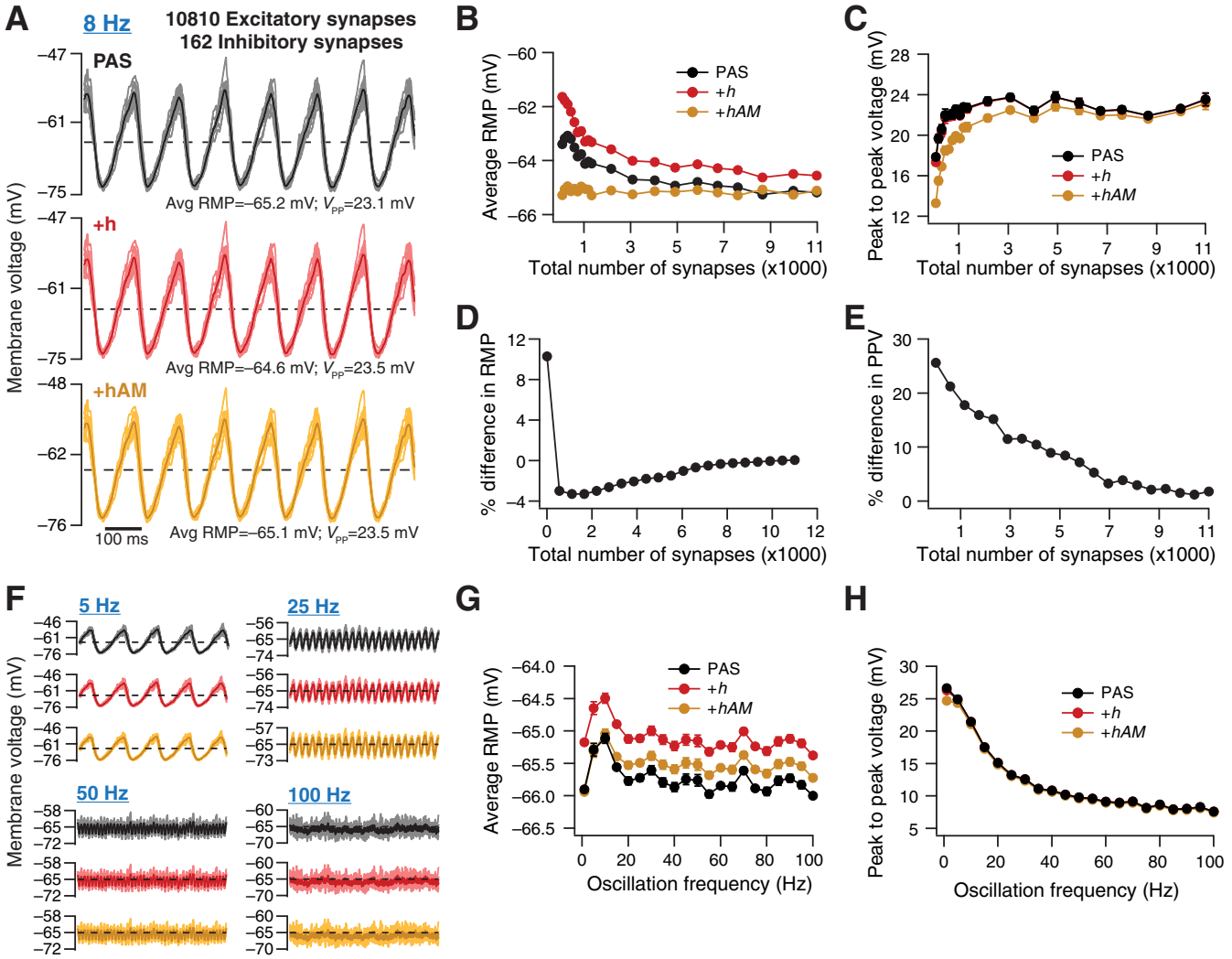

Fig. 10. Rhythmic high-conductance states, achieved under balanced excitatory and inhibitory synaptic inputs, tempered the efficacy of current- and conductance-based changes introduced by HCN channels. *A*: voltage traces recorded from the soma through different trials (n = 10; thin traces) and their average (thick trace), obtained in response to theta-modulated periodic synaptic inputs (8 Hz). Traces are shown for different channel configurations with balanced excitation-inhibition achieved through synaptic bombardment from 10,810 excitatory synapses and 162 inhibitory synapses distributed across the somatodendritic arbor. Avg, average. *B* and *C*: average RMP (*B*) and peak-to-peak voltage (PPV; *C*) plotted as functions of total number of synapses, for different channel configurations. The average RMP in response to 8-Hz periodic synaptic inputs was computed by time-averaging the trial-averaged voltage traces, and the overall PPV value was computed by averaging individual values of PPV computed across trials. *D* and *E*: percent differences in RMP (*D*) and PPV (*E*) plotted as functions of total number of synapses. Differences were computed between the PAS and +*hAM* configurations. *F*: voltage traces recorded from the soma through different trials (n = 10; thin traces) and their average (thick trace), obtained in response to periodic synaptic inputs at various frequencies. Traces are shown for different channel configurations, with synaptic numbers and distributions as shown in *A*. *G* and *H*: average RMP (*G*) and PPV (*H*) plotted as functions of oscillatory frequency, depicted for different channel configurations.

that the balance was with reference to the case where all channels were present (Fig. 10*B*). Importantly, and consistent with our previous observations (Figs. 3–9), we found that the average RMP values across different channel combinations progressively converged to the same value with an increase in number of synapses (Fig. 10, *B* and *D*). In other words, the differences in average RMP consequent to variations in channel configuration were significantly suppressed when the neuron switched to a periodic high-conductance state.

Because the measurement of R_{in}, a steady-state measure of neuronal excitability, was precluded by the presence of rhythmic inputs, we employed PPV amplitude of membrane potential oscillations as a measure of excitability and assessed average PPV under various channel and synaptic configurations (Fig. 10*C*). Consistent with our previous results using R_{in} or firing rate as measures of excitability (Figs. 3–9), we found that alterations to channel configurations led to differences in excitability when lesser numbers of synapses were present; however, these differences were significantly suppressed under periodic high-conductance states (Fig. 10, *C* and *E*). Finally, we varied the frequency of the oscillatory inputs that were employed to impart high-conductance states and found that the average RMP and the PPV were largely invariant to channel configurations under rhythmic high-conductance states achieved at different frequencies (Fig. 10, *F–H*). Together, these results demonstrated that the differences in RMP and excitability imposed by different channel configurations were significantly suppressed under rhythmic high-conductance states, where syn-

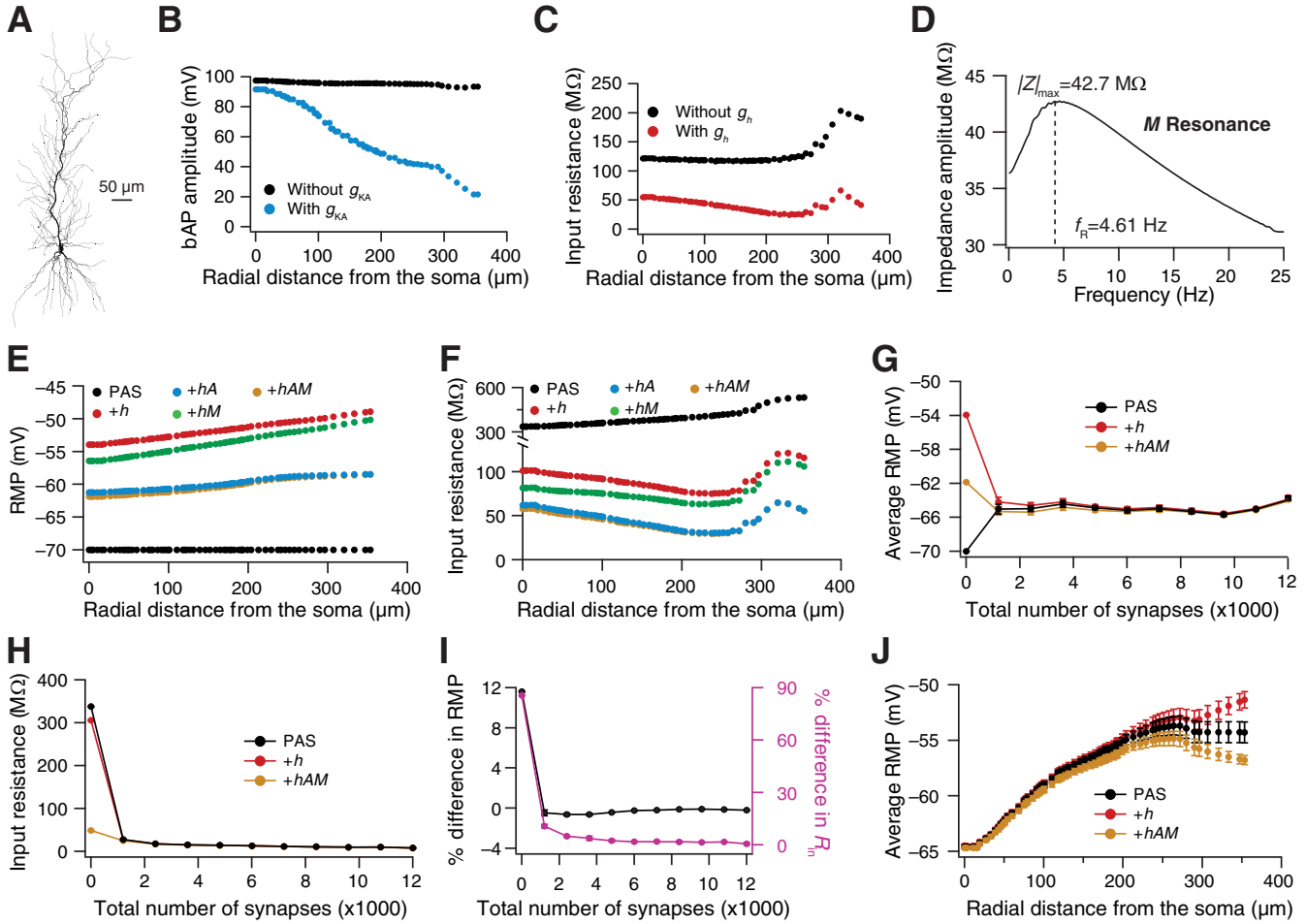

Fig. 11. KA channels and high-conductance state regulated the efficacy of current- and conductance-based changes introduced by HCN channels in a different morphological reconstruction. Parametric values were g_h^{Base} = 50 μS/cm², F_h = 100, x_h = 200 μm, k_h = 7 μm, g_{KA}^{base} = 3 mS/cm², F_{KA} = 5, $\bar{g}_{Na}$ = 12 mS/cm², R_a = 200 Ω·cm, R_m^{soma} = 20 kΩ·cm², R_m^{end} = 2,500 kΩ·cm², x_d = 50 μm, and k_{rm} = 10 μm. Note that these parameters (for reconstruction *ri04*) were different from those employed for simulations performed with the morphological reconstruction *n123* shown in Fig. 1*A*. These were consequent to the morphological differences, including changes in total dendritic length (*ri04*, 10.9 mm; *n123*, 17.6 mm), length of the somatoapical trunk (*ri04*, ~350 μm; *n123*, ~425 μm), and differences in branching structure. *A*: 2-dimensional projection of a 3-dimensional reconstructed hippocampal CA1 pyramidal neuron model. *B*: bAP amplitude plotted as a function of radial distance from the soma, in the presence and absence of KA channels, with HCN and KM channels inserted. *C*: R_{in} plotted as a function of radial distance from the soma, in the presence and absence of HCN channels, with KA and KM channels included. *D*: impedance amplitude profile, obtained from traces shown in Fig. 1*D*. *E* and *F*: RMP (*E*) and R_{in} (*F*) plotted as a function of radial distance along the somatoapical trunk for a passive model (PAS) and for models with the independent or co-insertion of HCN channels (+*h*, +*hM*, +*hAM*). *G* and *H*: average RMP (*G*) and R_{in} (*H*) plotted as functions of total number of synapses for different channel configurations. *I*: percent differences in RMP and R_{in} plotted as functions of total (excitatory + 40P-60D inhibitory) number of synapses. Differences were computed between the PAS and +*hAM* configurations. *J*: average RMP plotted as a function of radial distance from the soma for different channel configurations.

aptic currents and conductances play dominant roles in driving both RMP and excitability.

The regulation of HCN conductance-current balance by KA channels and high-conductance state was robust to change in the morphological reconstruction. We had employed a single morphological reconstruction of a hippocampal pyramidal neuron (Fig. 1*A*) for our simulations thus far. Were our results specific to only this morphology, or would they extend to other morphological reconstructions? To address this question, we repeated our experiments (in Figs. 2 and 4) with another morphological reconstruction (Fig. 11*A*) of a CA1 pyramidal neuron (Ascoli et al. 2007; Golding et al. 2005). First, we tuned the active and passive parameters of the model such that the baseline functional properties matched their physiological counterparts (Fig. 11, *B–D*; cf. Fig. 1, *B*, *C*, and *E*). Using this model, we found that co-insertion of KA channels with HCN channels tilted the HCN conductance-current balance heavily toward conductance by suppressing *h* current-induced RMP changes (Fig. 11*E*; cf. Fig. 2*C*) and enhancing HCN conductance-induced changes in R_{in} (Fig. 11*F*; cf. Fig. 2*E*). We then added balanced excitatory and inhibitory synapses after tuning their distance-invariant unitary somatic amplitudes to be ~0.2 and ~1 mV, respectively. We found that the addition of incrementally larger numbers of synapses significantly suppressed HCN channel-induced changes in both RMP and R_{in} (Fig. 11, *G–I*; cf. Fig. 6, *B*, *D*, and *F*, 40P-60D configuration), with synaptic currents and conductances dominating under such high-conductance states. Finally, when we looked at the distance-dependent average RMP values, we found that the dendrites were significantly more depolarized under high-conductance states and that KA channels can play a significant role in suppressing this depolarization (Fig. 11*J*; cf. Fig. 6*H*).

Together, our simulations with an additional morphological reconstruction confirmed our earlier results on how KA channels and high-conductance states could regulate the HCN conductance-current balance.

DISCUSSION

The prime conclusion of this study is that A-type K^+ channels and high-conductance states could act as effective and powerful regulators of the conductance-current balance that is triggered by the presence of HCN channels on neuronal membrane. We employed changes in RMP and R_{in} as measures of the impact of the *h* current and the HCN conductance, respectively, and assessed this conductance-current balance through several measures of excitability, including firing rate (Fig. 7) and peak voltage response to rhythmic inputs (Fig. 10). With reference to the roles of KA channels in regulating the conductance-current balance, we performed systematic sensitivity analyses spanning several active and passive parametric combinations (Figs. 2 and 5), sub- and suprathreshold neuronal states (Figs. 2, 5, and 7), different types of models for the KA channels (Figs. 2, 8, and 9), and different morphological reconstructions (Figs. 2 and 11). Our results, spanning all these parametric configurations, reveal that the co-insertion of KA channels with HCN channels significantly tilt the conductance-current balance in favor of conductance, thereby imparting an overall restorative effect on neuronal excitability. This tilt expresses by suppressing the impact of the inward *h* current in depolarizing the membrane potential and by enhancing the impact of the HCN conductance in reducing R_{in} and other measures of excitability (Figs. 2, 5, 7–9, and 11). In analyzing the role of high-conductance states in regulating this balance, our sensitivity analyses spanned all parameters mentioned with reference to KA channels above (Figs. 2, 5, 7–9, and 11) and revealed the robustness of our conclusions to balanced vs. unbalanced high-conductance states (Figs. 3 and 4), to changes in somatodendritic distribution of inhibitory synapses (Fig. 6), and to aperiodic vs. rhythmic (of several oscillatory frequencies) high-conductance states (Figs. 4 and 10). In doing this, we found that high-conductance states significantly suppress the impact of HCN-channel insertion on RMP and on all assessed measures of neuronal gain (R_{in}, firing rate, peak voltage response) and that synaptic conductances and currents dominate under such high-conductance states. In what follows, we present some implications of our results for HCN-channel physiology and their impact on neuronal function.

The twin gradients in KA and HCN channels form an ideal substrate to confer an overall restorative influence on somatodendritic excitability. A recent study involving HCN channels (Migliore and Migliore 2012) introduced a hypothetical leak conductance with specific constraints to elucidate the restorative properties of the inward *h* current. Important constraints on the hypothetical conductance required that its reversal potential be lower than RMP, that its somatodendritic distribution follows that of HCN channels, and that it should not inactivate with depolarization in the subthreshold range (Migliore and Migliore 2012). We submit that the KA channels reverse at K^+ reversal, which is typically hyperpolarized to RMP, that they exhibit a somatodendritic gradient that increases with distance from the soma, similar to that of HCN channels, and that despite being inactivating channels, they act very similar to leak channels in the subthreshold range as a direct consequence of the large window component in their voltage-dependent profile (Hoffman et al. 1997; Rathour and Narayanan 2012a). Furthermore, as subthreshold K^+ channels, they suppress the depolarization in RMP consequent to the inward *h* current and augment the role of HCN conductance in reducing excitability by contributing additional open channels at rest (Fig. 2, 5, 7–9, and 11). Therefore, upon co-insertion with HCN channels, the KA channels tilt the HCN channel-induced conductance-current balance heavily toward conductance. Taking these findings together, we postulate that the KA channel is a candidate mechanism that would fulfill the requirements of a hypothetical channel proposed by (Migliore and Migliore 2012), eliciting an overall restorative influence on neuronal excitability. Such a role for the KA channels is consistent with several studies that demonstrated the impact of the KA-channel window component on excitability (Hoffman et al. 1997; Johnston et al. 2003; Kim et al. 2005; Rathour and Narayanan 2012a, 2014), in vitro models of epilepsy consequent to the blockade of KA channels (Gonzalez-Sulser et al. 2011), and the expression of a HCN channel-dependent postinhibitory rebound in the absence of KA channels (Ascoli et al. 2010). Finally, the coexpression of HCN and KA channels spans a large variety of systems and have even been shown to be homeostatically coregulated, suggesting that the coexpression of these two channels plays an important role in regulating neuronal physiology (Amendola et al. 2012; Ascoli et al. 2010; MacLean et al. 2003; Santoro and Baram 2003).

Factors regulating HCN channel physiology under low- and high-conductance states. Our results demonstrate that under in vivo-like high-conductance states achieved through randomized synaptic activation, HCN channels play a subordinate role to afferent synaptic drive in specifying neuronal resting properties and excitability. These results suggest that the in vitro-centric debate on the role of HCN channels in excitability should reassess the dichotomous effects of HCN channels on excitability after accounting for in vivo-like conditions, where the dichotomy is largely overridden by afferent synaptic drive. Because the RMP under in vivo-like conditions is heavily dependent on the variable synaptic drive, electrophysiological experiments related to plasticity/modulation of HCN channels should record physiological measurements at multiple voltage levels, rather than focus on only two RMP values dictated by altered HCN channels under in vitro conditions. Furthermore, co-occurrence of plasticity in different ion channels is physiologically and pathophysiologically well established, and complex spatiotemporal interactions among different ion channels define response dynamics (Rathour and Narayanan 2012a, 2014; Santoro and Baram 2003). Therefore, it is essential to assess plasticity of different ion channels (and their interactions) across the somatodendritic arbor, in response to the same physiological/pathophysiological condition, before assigning a causal relationship between a restorative/regenerative change and the biophysics of a specific ion channel (Migliore and Migliore 2012; Santoro and Baram 2003).

What are the other potential candidates that could play a critical role in regulating the conductance-current balance introduced by HCN-channel expression? Our choice of analyzing A-type K^+ channels was consequent to the coexpression profiles of these channels with HCN channels across systems, and the choice to address the role of high-conductance states was to

ask if the in vitro-specific conclusions carried forward under in vivo-like conditions. However, hippocampal neurons express several other conductances that are active in the voltage range where HCN channels are active. Prominent among these are the L-, N- and T-type Ca^{2+} channels, the G protein-coupled inward rectifying K^+ (GIRK) channels, and the small-conductance Ca^{2+}-activated K^+ (SK) channels (Adelman et al. 2012; Chen and Johnston 2004; Lujan et al. 2009; Magee and Johnston 1995a; Santoro and Baram 2003; Tsay et al. 2007). Although the subcellular expression profiles of these channels are different from each other, future studies should explore spatial and kinetic interactions among these channels with the HCN conductance (Rathour and Narayanan 2012a, 2012b, 2014; Santoro and Baram 2003) in regulating the conductance-current balance.

The other potential regulators of the balance are the neuromodulatory inputs, which are known to regulate several synaptic receptors and voltage-gated ion channels through several signaling pathways (Adelman et al. 2012; Cantrell and Catterall 2001; He et al. 2014; Hoffman and Johnston 1999; Hofmann et al. 2014; Lujan et al. 2009; Marder and Thirumalai 2002; Munsch and Pape 1999; Perez-Reyes 2003; Robinson and Siegelbaum 2003; Rosenkranz and Johnston 2006, 2007), and the ability of passive, active, and morphological neuronal properties in modulating the shape of synaptic potentials (Andrasfalvy et al. 2008; Golding et al. 2005; Magee 2000; Magee and Johnston 1995b; Narayanan and Chattarji 2010; Perez-Rosello et al. 2011; Rall 1977; Spruston 2008; Stuart and Spruston 1998; Vetter et al. 2001; Williams and Stuart 2003). Specifically, neuromodulatory inputs could alter the HCN conductance-current balance through the regulation of voltage- and/or ligand-gated ion channels, thereby changing the manner in which the balance alters neuronal physiology.

Additionally, future studies should also assess the role of the morphology of the structure that these channels reside as a potential regulator of the HCN conductance-current balance. Specifically, neuronal morphology and associated microstructures, including dendritic diameter and branch-point structure, are well-established regulators of neuronal excitability and signal propagation (Ferrante et al. 2013; Krichmar et al. 2002; Mainen and Sejnowski 1996; Narayanan and Chattarji 2010; Schaefer et al. 2003; van Elburg and van Ooyen 2010; van Ooyen et al. 2002; Vetter et al. 2001). For instance, it is known that even identical somatodendritic distribution of ion channels lead to very different neuronal firing patterns and excitability, apart from altering backpropagating action potentials (Mainen and Sejnowski 1996; Narayanan and Chattarji 2010; Vetter et al. 2001). Therefore, it stands to reason the expression of the same set of ion channels would result in differential modulation of the HCN conductance-current balance in neurons with different morphologies and associated microstructures. Together, the impact of HCN channels on neuronal physiology should be analyzed in a state-dependent manner (Santoro and Baram 2003), accounting for the subcellular coexpression profile of different ion channels, the numbers and activation patterns of excitatory inhibitory synaptic inputs that these compartments receive, the interactive influences of neuromodulators and activity-dependent plasticity in several ion channels and receptors, and the morphology of the structure that these channels and receptors reside in.

Finally, it is critical that HCN channels are not analyzed only from a limited perspective of how they alter excitability. Specifically, the reason behind the unique conductance-current balance triggered by the presence of HCN channels is that they mediate an inward current that is active at rest. When viewed through the lens of how neurons respond to oscillatory inputs, this slow, hyperpolarization-activated depolarizing current active at rest forms the very reason behind HCN channels mediating a subthreshold resonating conductance (Hutcheon and Yarom 2000; Narayanan and Johnston 2008). As resonating conductances, HCN channels confer theta-frequency selectivity and an inductive lead in the impedance phase upon neuronal compartments responding to oscillatory inputs (Hutcheon and Yarom 2000; Narayanan and Johnston 2008; Vaidya and Johnston 2013). The location-dependent expression (Kole et al. 2006; Lorincz et al. 2002; Magee 1998; Williams and Stuart 2000) and plasticity of HCN channels (Campanac et al. 2008; Fan et al. 2005; Narayanan et al. 2010; Narayanan and Johnston 2008, 2007; Shah 2014; Shah et al. 2010; Wang et al. 2003), in conjunction with this ability to alter subthreshold response dynamics, have led to several postulates on their physiological roles. The postulated roles for HCN channels include those as regulators of location-dependent optimal filters (Kalmbach et al. 2013; Narayanan and Johnston 2007), of temporal summation and temporal coding (Magee 1998, 2000; Magee and Cook 2000; Narayanan and Johnston 2008; Wang 2010), and of transfer impedance amplitude and phase (Hu et al. 2009; Ulrich 2002; Vaidya and Johnston 2013), and as mediators of spectral selectivity in spike initiation dynamics (Das and Narayanan 2014) and of metaplasticity by altering synaptic plasticity rules (Honnuraiah and Narayanan 2013; Narayanan and Johnston 2010; Nolan et al. 2004). Against this wide array of potential roles, it is imperative that HCN channels are not analyzed only from a limited perspective of how they alter RMP and excitability. Importantly, the roles of HCN channels in altering intrinsic response dynamics and subthreshold oscillatory patterns, which are concurrent to the unique conductance-current balance they trigger, should especially be considered in brain regions such as the hippocampus where neurons are subjected to rhythmic high-conductance states.

ACKNOWLEDGMENTS

We thank Dr. Daniel Johnston and members of the cellular neurophysiology laboratory for helpful discussions.

GRANTS

This work was supported by the International Human Frontier Science Program Organization and the Department of Biotechnology through the US-India Brain Research Collaborative Program.

DISCLOSURES

No conflicts of interest, financial or otherwise, are declared by the authors.

AUTHOR CONTRIBUTIONS

P.M. and R.N. conception and design of research; P.M. and R.N. performed experiments; P.M. and R.N. analyzed data; P.M. and R.N. interpreted results of experiments; P.M. and R.N. prepared figures; P.M. and R.N. drafted manuscript; P.M. and R.N. edited and revised manuscript; P.M. and R.N. approved final version of manuscript.

REFERENCES

Adelman JP, Maylie J, Sah P. Small-conductance Ca^{2+}-activated K^+ channels: form and function. *Annu Rev Physiol* 74: 245–269, 2012.

Amarillo Y, De Santiago-Castillo JA, Dougherty K, Maffie J, Kwon E, Covarrubias M, Rudy B. Ternary Kv4.2 channels recapitulate voltage-dependent inactivation kinetics of A-type K^+ channels in cerebellar granule neurons. *J Physiol* 586: 2093–2106, 2008.

Amendola J, Woodhouse A, Martin-Eauclaire MF, Goaillard JM. Ca^{2+}/cAMP-sensitive covariation of I_A and I_H voltage dependences tunes rebound firing in dopaminergic neurons. *J Neurosci* 32: 2166–2181, 2012.

Andrasfalvy BK, Makara JK, Johnston D, Magee JC. Altered synaptic and non-synaptic properties of CA1 pyramidal neurons in Kv4.2 KO mice. *J Physiol* 586: 3881–3892, 2008.

Ascoli GA, Donohue DE, Halavi M. NeuroMorpho.Org: a central resource for neuronal morphologies. *J Neurosci* 27: 9247–9251, 2007.

Ascoli GA, Gasparini S, Medinilla V, Migliore M. Local control of postinhibitory rebound spiking in CA1 pyramidal neuron dendrites. *J Neurosci* 30: 6434–6442, 2010.

Bittner KC, Andrasfalvy BK, Magee JC. Ion channel gradients in the apical tuft region of CA1 pyramidal neurons. *PLoS One* 7: e46652, 2012.

Brager DH, Akhavan AR, Johnston D. Impaired dendritic expression and plasticity of h-channels in the *fmr1*$^{-/y}$ mouse model of fragile X syndrome. *Cell Rep* 1: 225–233, 2012.

Brager DH, Johnston D. Plasticity of intrinsic excitability during long-term depression is mediated through mGluR-dependent changes in I_h in hippocampal CA1 pyramidal neurons. *J Neurosci* 27: 13926–13937, 2007.

Breton JD, Stuart GJ. Loss of sensory input increases the intrinsic excitability of layer 5 pyramidal neurons in rat barrel cortex. *J Physiol* 587: 5107–5119, 2009.

Buhl EH, Halasy K, Somogyi P. Diverse sources of hippocampal unitary inhibitory postsynaptic potentials and the number of synaptic release sites. *Nature* 368: 823–828, 1994.

Buzsáki G. *Rhythms of the Brain*. New York: Oxford University Press, 2006.

Buzsáki G. Theta oscillations in the hippocampus. *Neuron* 33: 325–340, 2002.

Campanac E, Daoudal G, Ankri N, Debanne D. Downregulation of dendritic I_h in CA1 pyramidal neurons after LTP. *J Neurosci* 28: 8635–8643, 2008.

Cantrell AR, Catterall WA. Neuromodulation of Na^+ channels: an unexpected form of cellular plasticity. *Nat Rev Neurosci* 2: 397–407, 2001.

Carnevale NT, Hines ML. *The NEURON Book*. Cambridge, UK: Cambridge University Press, 2006.

Chance FS, Abbott LF, Reyes AD. Gain modulation from background synaptic input. *Neuron* 35: 773–782, 2002.

Chen K, Aradi I, Thon N, Eghbal-Ahmadi M, Baram TZ, Soltesz I. Persistently modified h-channels after complex febrile seizures convert the seizure-induced enhancement of inhibition to hyperexcitability. *Nat Med* 7: 331–337, 2001.

Chen X, Johnston D. Properties of single voltage-dependent K^+ channels in dendrites of CA1 pyramidal neurones of rat hippocampus. *J Physiol* 559: 187–203, 2004.

Chen X, Yuan LL, Zhao C, Birnbaum SG, Frick A, Jung WE, Schwarz TL, Sweatt JD, Johnston D. Deletion of Kv4.2 gene eliminates dendritic A-type K^+ current and enhances induction of long-term potentiation in hippocampal CA1 pyramidal neurons. *J Neurosci* 26: 12143–12151, 2006.

Csicsvari J, Hirase H, Czurko A, Mamiya A, Buzsáki G. Oscillatory coupling of hippocampal pyramidal cells and interneurons in the behaving Rat. *J Neurosci* 19: 274–287, 1999.

Das A, Narayanan R. Active dendrites regulate spectral selectivity in location-dependent spike initiation dynamics of hippocampal model neurons. *J Neurosci* 34: 1195–1211, 2014.

Destexhe A, Rudolph M, Pare D. The high-conductance state of neocortical neurons in vivo. *Nat Rev Neurosci* 4: 739–751, 2003.

Domnisoru C, Kinkhabwala AA, Tank DW. Membrane potential dynamics of grid cells. *Nature* 495: 199–204, 2013.

Dyhrfjeld-Johnsen J, Morgan RJ, Soltesz I. Double trouble? Potential for hyperexcitability following both channelopathic up- and downregulation of I_h in epilepsy. *Front Neurosci* 3: 25–33, 2009.

Fan Y, Fricker D, Brager DH, Chen X, Lu HC, Chitwood RA, Johnston D. Activity-dependent decrease of excitability in rat hippocampal neurons through increases in I_h. *Nat Neurosci* 8: 1542–1551, 2005.

Ferrante M, Migliore M, Ascoli GA. Functional impact of dendritic branch-point morphology. *J Neurosci* 33: 2156–2165, 2013.

Fineberg JD, Ritter DM, Covarrubias M. Modeling-independent elucidation of inactivation pathways in recombinant and native A-type Kv channels. *J Gen Physiol* 140: 513–527, 2012.

Gasparini S, DiFrancesco D. Action of the hyperpolarization-activated current (I_h) blocker ZD 7288 in hippocampal CA1 neurons. *Pflügers Arch* 435: 99–106, 1997.

George MS, Abbott LF, Siegelbaum SA. HCN hyperpolarization-activated cation channels inhibit EPSPs by interactions with M-type K^+ channels. *Nat Neurosci* 12: 577–584, 2009.

Golding NL, Mickus TJ, Katz Y, Kath WL, Spruston N. Factors mediating powerful voltage attenuation along CA1 pyramidal neuron dendrites. *J Physiol* 568: 69–82, 2005.

Gonzalez-Sulser A, Wang J, Motamedi GK, Avoli M, Vicini S, Dzakpasu R. The 4-aminopyridine in vitro epilepsy model analyzed with a perforated multi-electrode array. *Neuropharmacology* 60: 1142–1153, 2011.

Harvey CD, Collman F, Dombeck DA, Tank DW. Intracellular dynamics of hippocampal place cells during virtual navigation. *Nature* 461: 941–946, 2009.

He C, Chen F, Li B, Hu Z. Neurophysiology of HCN channels: from cellular functions to multiple regulations. *Prog Neurobiol* 112: 1–23, 2014.

Hodgkin AL, Huxley AF. A quantitative description of membrane current and its application to conduction and excitation in nerve. *J Physiol* 117: 500–544, 1952.

Hoffman DA, Johnston D. Neuromodulation of dendritic action potentials. *J Neurophysiol* 81: 408–411, 1999.

Hoffman DA, Magee JC, Colbert CM, Johnston D. K^+ channel regulation of signal propagation in dendrites of hippocampal pyramidal neurons. *Nature* 387: 869–875, 1997.

Hofmann F, Flockerzi V, Kahl S, Wegener JW. L-type $Ca_V1.2$ calcium channels: from in vitro findings to in vivo function. *Physiol Rev* 94: 303–326, 2014.

Honnuraiah S, Narayanan R. A calcium-dependent plasticity rule for HCN channels maintains activity homeostasis and stable synaptic learning. *PLoS One* 8: e55590, 2013.

Hu H, Vervaeke K, Graham LJ, Storm JF. Complementary theta resonance filtering by two spatially segregated mechanisms in CA1 hippocampal pyramidal neurons. *J Neurosci* 29: 14472–14483, 2009.

Hu H, Vervaeke K, Storm JF. M-channels (Kv7/KCNQ channels) that regulate synaptic integration, excitability, and spike pattern of CA1 pyramidal cells are located in the perisomatic region. *J Neurosci* 27: 1853–1867, 2007.

Hu H, Vervaeke K, Storm JF. Two forms of electrical resonance at theta frequencies, generated by M-current, h-current and persistent Na^+ current in rat hippocampal pyramidal cells. *J Physiol* 545: 783–805, 2002.

Hutcheon B, Yarom Y. Resonance, oscillation and the intrinsic frequency preferences of neurons. *Trends Neurosci* 23: 216–222, 2000.

Johnston D, Christie BR, Frick A, Gray R, Hoffman DA, Schexnayder LK, Watanabe S, Yuan LL. Active dendrites, potassium channels and synaptic plasticity. *Philos Trans R Soc Lond B Biol Sci* 358: 667–674, 2003.

Jung S, Jones TD, Lugo JN Jr, Sheerin AH, Miller JW, D'Ambrosio R, Anderson AE, Poolos NP. Progressive dendritic HCN channelopathy during epileptogenesis in the rat pilocarpine model of epilepsy. *J Neurosci* 27: 13012–13021, 2007.

Kalmbach BE, Chitwood RA, Dembrow NC, Johnston D. Dendritic generation of mGluR-mediated slow afterdepolarization in layer 5 neurons of prefrontal cortex. *J Neurosci* 33: 13518–13532, 2013.

Kim CS, Chang PY, Johnston D. Enhancement of dorsal hippocampal activity by knockdown of HCN1 channels leads to anxiolytic- and antidepressant-like behaviors. *Neuron* 75: 503–516, 2012.

Kim J, Wei DS, Hoffman DA. Kv4 potassium channel subunits control action potential repolarization and frequency-dependent broadening in rat hippocampal CA1 pyramidal neurones. *J Physiol* 569: 41–57, 2005.

Klausberger T, Magill PJ, Márton LF, Roberts JD, Cobden PM, Buzsáki G, Somogyi P. Brain-state- and cell-type-specific firing of hippocampal interneurons in vivo. *Nature* 421: 844–848, 2003.

Klausberger T, Somogyi P. Neuronal diversity and temporal dynamics: the unity of hippocampal circuit operations. *Science* 321: 53–57, 2008.

Kole MH, Brauer AU, Stuart GJ. Inherited cortical HCN1 channel loss amplifies dendritic calcium electrogenesis and burst firing in a rat absence epilepsy model. *J Physiol* 578: 507–525, 2007.

Kole MH, Hallermann S, Stuart GJ. Single I_h channels in pyramidal neuron dendrites: properties, distribution, and impact on action potential output. *J Neurosci* 26: 1677–1687, 2006.

Krichmar JL, Nasuto SJ, Scorcioni R, Washington SD, Ascoli GA. Effects of dendritic morphology on CA3 pyramidal cell electrophysiology: a simulation study. *Brain Res* 941: 11–28, 2002.

Lerche H, Shah M, Beck H, Noebels J, Johnston D, Vincent A. Ion channels in genetic and acquired forms of epilepsy. *J Physiol* 591: 753–764, 2013.

Lewis AS, Vaidya SP, Blaiss CA, Liu Z, Stoub TR, Brager DH, Chen X, Bender RA, Estep CM, Popov AB, Kang CE, Van Veldhoven PP, Bayliss DA, Nicholson DA, Powell CM, Johnston D, Chetkovich DM. Deletion of the hyperpolarization-activated cyclic nucleotide-gated channel auxiliary subunit TRIP8b impairs hippocampal I_h localization and function and promotes antidepressant behavior in mice. *J Neurosci* 31: 7424–7440, 2011.

Lippert A, Booth V. Understanding effects on excitability of simulated I_h modulation in simple neuronal models. *Biol Cybern* 101: 297–306, 2009.

Lorincz A, Notomi T, Tamas G, Shigemoto R, Nusser Z. Polarized and compartment-dependent distribution of HCN1 in pyramidal cell dendrites. *Nat Neurosci* 5: 1185–1193, 2002.

Lujan R, Maylie J, Adelman JP. New sites of action for GIRK and SK channels. *Nat Rev Neurosci* 10: 475–480, 2009.

MacLean JN, Zhang Y, Johnson BR, Harris-Warrick RM. Activity-independent homeostasis in rhythmically active neurons. *Neuron* 37: 109–120, 2003.

Magee JC. Dendritic hyperpolarization-activated currents modify the integrative properties of hippocampal CA1 pyramidal neurons. *J Neurosci* 18: 7613–7624, 1998.

Magee JC. Dendritic integration of excitatory synaptic input. *Nat Rev Neurosci* 1: 181–190, 2000.

Magee JC, Cook EP. Somatic EPSP amplitude is independent of synapse location in hippocampal pyramidal neurons. *Nat Neurosci* 3: 895–903, 2000.

Magee JC, Johnston D. Characterization of single voltage-gated Na^+ and Ca^{2+} channels in apical dendrites of rat CA1 pyramidal neurons. *J Physiol* 487: 67–90, 1995a.

Magee JC, Johnston D. Synaptic activation of voltage-gated channels in the dendrites of hippocampal pyramidal neurons. *Science* 268: 301–304, 1995b.

Mainen ZF, Sejnowski TJ. Influence of dendritic structure on firing pattern in model neocortical neurons. *Nature* 382: 363–366, 1996.

Marder E, Thirumalai V. Cellular, synaptic and network effects of neuromodulation. *Neural Netw* 15: 479–493, 2002.

Megias M, Emri Z, Freund TF, Gulyas AI. Total number and distribution of inhibitory and excitatory synapses on hippocampal CA1 pyramidal cells. *Neuroscience* 102: 527–540, 2001.

Migliore M, Hoffman DA, Magee JC, Johnston D. Role of an A-type K^+ conductance in the back-propagation of action potentials in the dendrites of hippocampal pyramidal neurons. *J Comput Neurosci* 7: 5–15, 1999.

Migliore M, Migliore R. Know your current I*h*: interaction with a shunting current explains the puzzling effects of its pharmacological or pathological modulations. *PLoS One* 7: e36867, 2012.

Munsch T, Pape HC. Modulation of the hyperpolarization-activated cation current of rat thalamic relay neurones by intracellular pH. *J Physiol* 519: 493–504, 1999.

Narayanan R, Chattarji S. Computational analysis of the impact of chronic stress on intrinsic and synaptic excitability in the hippocampus. *J Neurophysiol* 103: 3070–3083, 2010.

Narayanan R, Dougherty KJ, Johnston D. Calcium store depletion induces persistent perisomatic increases in the functional density of h channels in hippocampal pyramidal neurons. *Neuron* 68: 921–935, 2010.

Narayanan R, Johnston D. Functional maps within a single neuron. *J Neurophysiol* 108: 2343–2351, 2012.

Narayanan R, Johnston D. The h channel mediates location dependence and plasticity of intrinsic phase response in rat hippocampal neurons. *J Neurosci* 28: 5846–5860, 2008.

Narayanan R, Johnston D. The *h* current is a candidate mechanism for regulating the sliding modification threshold in a BCM-like synaptic learning rule. *J Neurophysiol* 104: 1020–1033, 2010.

Narayanan R, Johnston D. Long-term potentiation in rat hippocampal neurons is accompanied by spatially widespread changes in intrinsic oscillatory dynamics and excitability. *Neuron* 56: 1061–1075, 2007.

Noam Y, Bernard C, Baram TZ. Towards an integrated view of HCN channel role in epilepsy. *Curr Opin Neurobiol* 21: 873–879, 2011.

Nolan MF, Malleret G, Dudman JT, Buhl DL, Santoro B, Gibbs E, Vronskaya S, Buzsáki G, Siegelbaum SA, Kandel ER, Morozov A. A behavioral role for dendritic integration: HCN1 channels constrain spatial memory and plasticity at inputs to distal dendrites of CA1 pyramidal neurons. *Cell* 119: 719–732, 2004.

Pape HC. Queer current and pacemaker: the hyperpolarization-activated cation current in neurons. *Annu Rev Physiol* 58: 299–327, 1996.

Pavlov I, Scimemi A, Savtchenko L, Kullmann DM, Walker MC. I_h-mediated depolarization enhances the temporal precision of neuronal integration. *Nat Commun* 2: 199, 2011.

Perez-Reyes E. Molecular physiology of low-voltage-activated T-type calcium channels. *Physiol Rev* 83: 117–161, 2003.

Perez-Rosello T, Baker JL, Ferrante M, Iyengar S, Ascoli GA, Barrionuevo G. Passive and active shaping of unitary responses from associational/commissural and perforant path synapses in hippocampal CA3 pyramidal cells. *J Comput Neurosci* 31: 159–182, 2011.

Poirazi P, Brannon T, Mel BW. Pyramidal neuron as two-layer neural network. *Neuron* 37: 989–999, 2003.

Poolos NP, Migliore M, Johnston D. Pharmacological upregulation of h-channels reduces the excitability of pyramidal neuron dendrites. *Nat Neurosci* 5: 767–774, 2002.

Pyapali GK, Sik A, Penttonen M, Buzsáki G, Turner DA. Dendritic properties of hippocampal CA1 pyramidal neurons in the rat: intracellular staining in vivo and in vitro. *J Comp Neurol* 391: 335–352, 1998.

Rall W. Core conductor theory and cable properties of neurons. In: *Handbook of Physiology. The Nervous System. Cellular Biology of Neurons*. Bethesda, MD: Am Physiol Soc, 1977, p. 39–97.

Rathour RK, Narayanan R. Homeostasis of functional maps in active dendrites emerges in the absence of individual channelostasis. *Proc Natl Acad Sci USA* 111: E1787–E1796, 2014.

Rathour RK, Narayanan R. Inactivating ion channels augment robustness of subthreshold intrinsic response dynamics to parametric variability in hippocampal model neurons. *J Physiol* 590: 5629–5652, 2012a.

Rathour RK, Narayanan R. Influence fields: a quantitative framework for representation and analysis of active dendrites. *J Neurophysiol* 107: 2313–2334, 2012b.

Robinson RB, Siegelbaum SA. Hyperpolarization-activated cation currents: from molecules to physiological function. *Annu Rev Physiol* 65: 453–480, 2003.

Rosenkranz JA, Johnston D. Dopaminergic regulation of neuronal excitability through modulation of I_h in layer V entorhinal cortex. *J Neurosci* 26: 3229–3244, 2006.

Rosenkranz JA, Johnston D. State-dependent modulation of amygdala inputs by dopamine-induced enhancement of sodium currents in layer V entorhinal cortex. *J Neurosci* 27: 7054–7069, 2007.

Santoro B, Baram TZ. The multiple personalities of h-channels. *Trends Neurosci* 26: 550–554, 2003.

Schaefer AT, Larkum ME, Sakmann B, Roth A. Coincidence detection in pyramidal neurons is tuned by their dendritic branching pattern. *J Neurophysiol* 89: 3143–3154, 2003.

Schmidt-Hieber C, Hausser M. Cellular mechanisms of spatial navigation in the medial entorhinal cortex. *Nat Neurosci* 16: 325–331, 2013.

Schomburg EW, Anastassiou CA, Buzsáki G, Koch C. The spiking component of oscillatory extracellular potentials in the rat hippocampus. *J Neurosci* 32: 11798–11811, 2012.

Shah MM. Cortical HCN channels: function, trafficking and plasticity. *J Physiol* 592: 2711–2719, 2014.

Shah MM. HCN1 channels: a new therapeutic target for depressive disorders? *Sci Signal* 5: pe44, 2012.

Shah MM, Anderson AE, Leung V, Lin X, Johnston D. Seizure-induced plasticity of h channels in entorhinal cortical layer III pyramidal neurons. *Neuron* 44: 495–508, 2004.

Shah MM, Hammond RS, Hoffman DA. Dendritic ion channel trafficking and plasticity. *Trends Neurosci* 33: 307–316, 2010.

Shah MM, Huang Z, Martinello K. HCN and KV7 (M-) channels as targets for epilepsy treatment. *Neuropharmacology* 69: 75–81, 2013.

Shah MM, Migliore M, Valencia I, Cooper EC, Brown DA. Functional significance of axonal Kv7 channels in hippocampal pyramidal neurons. *Proc Natl Acad Sci USA* 105: 7869–7874, 2008.

Spruston N. Pyramidal neurons: dendritic structure and synaptic integration. *Nat Rev Neurosci* 9: 206–221, 2008.

Stuart G, Spruston N. Determinants of voltage attenuation in neocortical pyramidal neuron dendrites. *J Neurosci* 18: 3501–3510, 1998.

Tsay D, Dudman JT, Siegelbaum SA. HCN1 channels constrain synaptically evoked Ca^{2+} spikes in distal dendrites of CA1 pyramidal neurons. *Neuron* 56: 1076–1089, 2007.

Ulrich D. Dendritic resonance in rat neocortical pyramidal cells. *J Neurophysiol* 87: 2753–2759, 2002.

Vaidya SP, Johnston D. Temporal synchrony and gamma-to-theta power conversion in the dendrites of CA1 pyramidal neurons. *Nat Neurosci* 16: 1812–1820, 2013.

van Elburg RA, van Ooyen A. Impact of dendritic size and dendritic topology on burst firing in pyramidal cells. *PLoS Comput Biol* 6: e1000781, 2010.

van Ooyen A, Duijnhouwer J, Remme MW, van Pelt J. The effect of dendritic topology on firing patterns in model neurons. *Network* 13: 311–325, 2002.

van Welie I, van Hooft JA, Wadman WJ. Homeostatic scaling of neuronal excitability by synaptic modulation of somatic hyperpolarization-activated I_h channels. *Proc Natl Acad Sci USA* 101: 5123–5128, 2004.

Vetter P, Roth A, Hausser M. Propagation of action potentials in dendrites depends on dendritic morphology. *J Neurophysiol* 85: 926–937, 2001.

Wang XJ. Neurophysiological and computational principles of cortical rhythms in cognition. *Physiol Rev* 90: 1195–1268, 2010.

Wang Z, Xu NL, Wu CP, Duan S, Poo MM. Bidirectional changes in spatial dendritic integration accompanying long-term synaptic modifications. *Neuron* 37: 463–472, 2003.

Williams SR, Stuart GJ. Role of dendritic synapse location in the control of action potential output. *Trends Neurosci* 26: 147–154, 2003.

Williams SR, Stuart GJ. Site independence of EPSP time course is mediated by dendritic I_h in neocortical pyramidal neurons. *J Neurophysiol* 83: 3177–3182, 2000.